Vietnam Journal of Earth Sciences, 47(4), 479–506, https://doi.org/10.15625/2615-9783/23628

Vietnam Journal of Earth Sciences
https://vjs.ac.vn/index.php/jse

P–T evolution and tectonothermal history of metamorphic rocks in Nam Dinh, the southeasternmost part of the Day Nui Con Voi metamorphic complex, Northern Vietnam

Ippei Kitano*[1], Vuong Bui Thi Sinh[1,2]

[1]*The Hokkaido University Museum, Hokkaido University, Hokkaido 060-0810, Japan*
[2]*Institute of Earth Sciences, Vietnam Academy of Science and Technology, Hanoi, Vietnam*

Received 19 July 2025; Received in revised form 23 September 2025; Accepted 15 October 2025

ABSTRACT

The Day Nui Con Voi high-grade metamorphic complex (DNCV) in northern Vietnam is considered the southeastern part of the Red River Shear Zone (RRSZ), a major tectonic boundary between the South China and Indochina Blocks. This study investigated minor outcrops in Nam Dinh, at the southeasternmost part of the complex, which are deficient in petrological research. It aims to establish the tectonic evolution based on the petrographic and structural features of pelitic schists and gneisses. Apart from sandstones found in the northern part, the petrographic observations reveal the metamorphic zonation from the chlorite zone, through the biotite-muscovite zone, to the sillimanite zone, progressing eastward with increasing metamorphic grade. The prominent subhorizontal mylonitic foliation (S2) folded by later open fold composes doming structure in study area. Pre-S2 microstructures (S0 and S1) and post-S2 myrmekite are also preserved. Geothermobarometric analyses of a pelitic schist in the chlorite zone and a gneiss in the sillimanite zone indicates a clockwise pressure-temperature path. The estimated metamorphic geothermal gradients are 20–25°C/km during the prograde stage, 30°C/km at peak granulite-facies metamorphism and *ca.* 60°C/km during retrograde conditions with the myrmekite formation. The petrological and structural characteristics are well comparable to those of the main body of the DNCV and the contemporaneous Bu Khang Dome (BKD). The combining thermal histories of the DNCV and the East Sea opening suggest the following regional tectonic evolution during Eocene-Oligocene. The Himalayan orogeny caused the crustal thickening in the DNCV and BKD on the prograde stage. Initial extensional magmatism and crustal thinning due to the onset of the East Sea opening in the back-arc setting triggered the granulite-facies metamorphism with extensive crustal anataxis, producing numerous syn-metamorphic leucogranites in the lower crust. Subsequent East Sea opening resulted in the extensional regime accompanied by the subhorizontal ductile deformation in the DNCV, and possibly in the BKD and the RRSZ. Crustal strike-slip shearing took place along the thinned and weakened anatectic crust and uplifted their metamorphic rocks with doming structure toward greenschist-facies upper crust. This process may have been correlated with the southward ridge jump of the East Sea.

Keywords: Day Nui Con Voi metamorphic complex, Red River Shear Zone, East Sea, Pressure-temperature evolution, Nam Dinh.

1. Introduction

The Red River Shear Zone (RRSZ) is one of the large-scale strike-slip faults, extending for over 1000 km from Tibet to the East Sea (e.g., Tapponnier et al., 1982; Nam et al., 1998) (Fig. 1a). It plays important roles in not

*Corresponding author, Email: kitano@museum.hokudai.ac.jp

only the Permo–Triassic continental collision between South China and Indochina Blocks as a part of the Trans Vietnam Orogenic Belt (Osanai et al., 2008) but also Cenozoic left-lateral strike-slip shear deformation driven by extrusion tectonics in response to the India-Asia collision (e.g., Tapponnier et al., 1982). Cenozoic shearing activity of the RRSZ was almost contemporaneous with the opening of the East Sea during *ca.* 32–17 Ma (e.g., Tapponnier et al., 1982; Gilley et al., 2003; Anczkiewicz et al., 2007; Mai et al., 2018; Dinh et al., 2023). Thus, the tectonic evolution of the RRSZ is a key factor in deciphering the growth process of the Asian continent in Southeast Asia. Traditionally, previous studies have suggested that left-lateral shearing along the RSSZ caused the seafloor spreading of the East Sea, based on the paleographic and geochronological coincidence in the Cenozoic (e.g., Tapponnier et al., 1982; Gilley et al., 2003). However, a recent study Dinh et al. (2023) reconstructed the metamorphic and deformational histories of the Day Nui Con Voi metamorphic complex (DNCV) in the southern part of the RRSZ (Figs. 1a-b). They proposed that the initial opening of the East Sea prior to the shearing of the RRSZ, which triggered the southward ridge jump of the East Sea. Therefore, the tectonic linkage between the RRSZ and the East Sea remains controversial, and establishing the precise timeline of the metamorphic and deformation processes in the RSSZ could be a key to resolving this debate.

The DNCV, mainly located between Lao Cai and Viet Tri in northern Vietnam, consists mainly of high-temperature (HT) metamorphic rocks (e.g., Nam et al, 1998). Numerous geological, petrological, and chronological studies have revealed the Cenozoic metamorphic and deformational history of the DNCV (Nam et al, 1998; Wang et al., 2000; Leloup et al., 2001; Gilley et al., 2003; Anczkiewicz et al., 2007; Yeh et al., 2008; Palin et al., 2013; Dinh et al., 2023 and references therein). They have described Oligocene to Early Miocene amphibolite- to granulite-facies metamorphism associated with pre- to syn-metamorphic granitic magmatism, three phases of ductile deformation, and terminative brittle fault movement within this metamorphic complex (Fig. 1b). However, the correlation between the detailed pressure (*P*)–temperature (*T*) conditions and deformation history has not yet been clarified in the DNCV. This lack of information on their metamorphic evolution will hinder a comprehensive understanding of the formation process for the DNCV, and by extension, the RRSZ. Furthermore, the minor equivalent outcrops distributed around Nam Dinh, representing the southeasternmost extension of the DNCV, have been poorly investigated. Some previous studies have briefly reported the lithologies, including garnet–sillimanite–biotite–muscovite gneiss, as well as the chronological and structural characteristics of the metamorphic rocks and granitoids in this area (Wang et al., 2000; Leloup et al., 2001; Gilley et al., 2003; Yeh et al., 2008). However, limited petrological analyses have been conducted to these metamorphic rocks. They have the potential to provide crucial hints for the metamorphic and deformational process related to the opening of the East Sea owing to their location closest to the East Sea in the DNCV (Fig. 1b). Therefore, we conducted systematic field survey, petrographical observation, and *P–T* estimation for pelitic metamorphic rocks in the small outcrops around Nam Dinh to clarify their petrological and structural correlation with the DNCV and their tectonothermal history involving the development of the East Sea. Mineral abbreviations used in Figures and Tables follow Warr (2021).

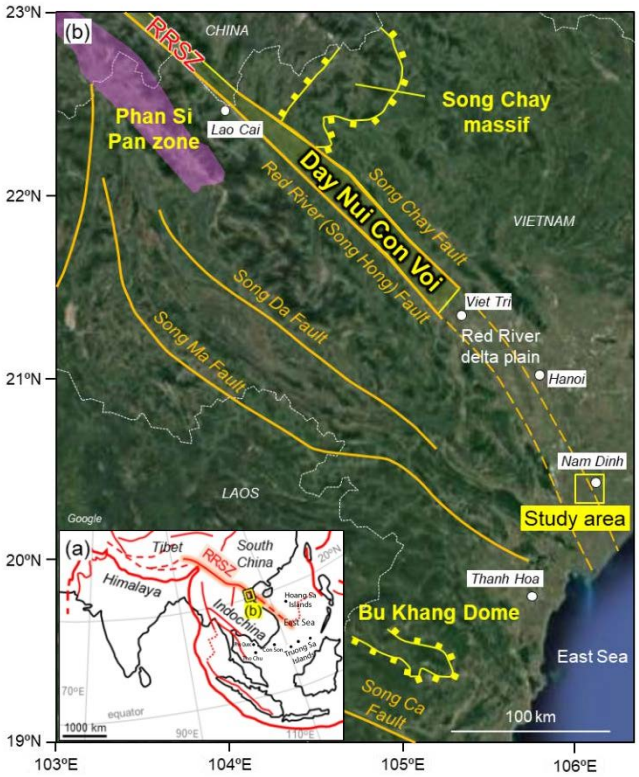

Figure 1. (a) Tectonic map in Southeast Asia after Tapponnier et al. (1982) and Anczkiewicz et al. (2007). Red bold and dotted lines depict major fault or plate boundaries and spreading axes, respectively. A small yellow box represents the area shown in (b). RRSZ: Red River Shear Zone. (b) Distribution of the Day Nui Con Voi metamorphic complex, Phan Si Pan zone, Song Chay massif, and Bu Khang Dome with major faults in north Vietnam after Jolivet et al. (2001) and Gilley et al. (2003). The study area is also shown here

2. Geological outline

The DNCV is located in the southeastern part of the NW–SE trending RRSZ, which is the largest strike-slip shear zone extending beyond 1000 km in Southeast Asia (e.g., Nam et al., 1998; Yeh et al., 2008). Extending from Lao Cai to Viet Tri city in northern Vietnam with 30 km wide and over 250 km long, it is widely covered by Neogene–Quaternary sediments of the Song Hong delta plain in the southern Viet Tri (Fig. 1b). Two steep normal faults of the Chay River Fault and Red River Fault bound the DNCV at the northside and southside, respectively (Nam et al., 1998). This metamorphic complex consists mainly of amphibolite- to granulite-facies metamorphic rocks, including amphibolite, mylonite, garnet–biotite ± sillimanite gneiss, mica schist, and minor marble (e.g., Nam et al., 1998; Yeh et al., 2008).

Several petrological and geothermobarometric studies have been carried out in the DNCV (Nam et al., 1998; Leloup et al., 2001; Gilley et al., 2003; Anczkiewicz et al., 2007; Palin et al., 2013). A pioneering study by Nam et al. (1998) proposed a clockwise *P–T* path, with peak amphibolite-facies metamorphism at *ca.* 6.5 kbar and 690°C, followed by greenschist-facies mylonitization at *ca.* 3 kbar and 480°C. The higher peak *P–T* conditions were also reported, including >700°C at *ca.* 6 kbar (Leloup et al., 2001), 780–830°C at *ca.* 7.5–8.8 kbar (Gilley et al., 2003),

810–820°C at *ca*. 5.6–7.0 kbar (Anczkiewicz et al., 2007), and 805°C at *ca.* 8.5 kbar with subsequent retrogression at 4–5 kbar and 640–700°C (Palin et al., 2013).

Yeh et al. (2008) proposed four deformation events in the DNCV, including the Nam Dinh area: upright folding (D_1), recumbent folding (D_2), doming (D_3), and a subsequent left-lateral faulting event (D_4). Dinh et al. (2023) updated the ductile deformation history based on their own dataset and compiled chronological results. They proposed NNW–SSE striking upright D_1 folding before 32 Ma at the peak upper amphibolite- to granulite-facies, subhorizontal D_2 recumbent folding during 32–26 Ma at post-peak amphibolite-facies, and syn-left lateral shearing D_3 doming event during *ca.* 26–22 Ma under retrograde greenschist-facies.

Radiometric geochronological studies using K–Ar and Ar–Ar dating methods in the DNCV revealed predominant Oligocene to Early Miocene metamorphic ages of *ca.* 37–17 Ma (e.g., Leloup et al., 1995, 2001; Nam et al., 1998; Trinh et al., 1998; Wang et al., 1998, 2000; Garnier et al., 2002; Duong et al., 2021). These ages are coeval with granitic magmatism, ruby and Cu–Au mineralization, possibly associated with the left-lateral strike-slip displacement along the RRSZ (Leloup et al., 1995, 2001; Nam et al., 1998; Trinh et al., 1998; Wang et al., 1998, 2000; Garnier et al., 2002; Duong et al., 2021). Some authors proposed that the RRSZ shearing acted since *ca.* 35 Ma and caused amphibolite-facies HT metamorphism by the shearing heating and some upward heat advection, which resulted in granitic magmatism through the crustal melting and ruby mineralization in marble (e.g., Leloup et al., 1995, 2001; Trinh et al., 1998; Garnier et al., 2002; Duong et al., 2021). On the other hand, Wang et al. (1998, 2000) revealed slow cooling from *ca.* 34 to 25 Ma at around 500°C and rapid cooling after 25 Ma during the exhumation of the DNCV. Based on the contemporaneous rapid cooling from approximately 27 to 17 Ma in the entire RSSZ, resulting from the sharing and priority of potassic magmatism at around 30 Ma, followed by RSSZ shearing (Chung et al., 1997), they suggested that the onset of displacement possibly occurred around 27 Ma. In-situ monazite U–Th–Pb isotope dating by Gilley et al. (2003) and Palin et al. (2013) indicated a thermal history of high-grade metamorphism at *ca.* 38–34 Ma, followed by retrograde with strike-slip shearing after *ca.* 31 Ma, and post-kinematic granite intrusion at *ca.* 25 Ma. Based on the zircon U–Pb ages, Chen et al. (2019) reported the Eocene to Oligocene granitic magmatism from granitic mylonite and mylonitized granitic dyke intruding the paragneiss in the northern extension of the DNCV in China.

3. Sample description

Around Nam Dinh, approximately 80 km south of Hanoi, some outcrops of metamorphic rocks occur sporadically on the Red River delta plain within the area of *ca.* 13 × 13 km^2 in the south (Fig. 2). In the northern part, small outcrops of sandstones are also discovered, with bedding planes striking E–W to NW–SE and dipping southward (Fig. 2). The metamorphic rocks consist of pelitic schists in the west and mylonitized pelitic gneisses in the east, which are intruded by subconcordant to discordant leucogranite and pegmatite (Fig. 2), along with rare thin mafic layers. The metamorphic foliation is characterized by various strikes and gentle dips (< 40°), with a N- to NW-trending subhorizontal lineation, consistently indicating top-to-the-N shear sense. The petrography of representative samples is described below.

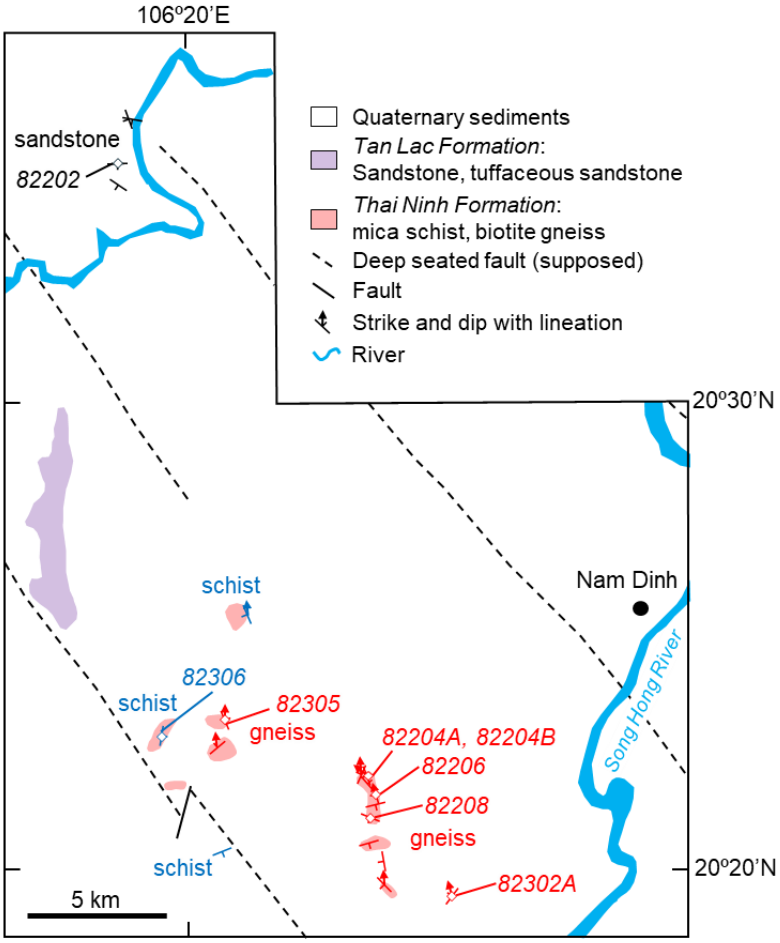

Figure 2. Simplified geological map around the Nam Dinh area after Hoang (1999) and Dinh (2004). Foliations with/without lineations are shown in black for sandstones, blue for schists, and red for gneisses. Diamond marks display the localities of described samples with sample numbers

3.1. Sandstone

The sandstone in the northern part of the study area exhibits bedding planes, which are cut by quartz veins (Fig. 3a). It mainly consists of fine-grained angular quartz, with subordinate sericite and muscovite, and accessory plagioclase, bluish to brownish tourmaline, and opaque minerals, including carbonaceous materials (CM) (Fig. 4a). Sandstones are locally folded.

3.2. Garnet–chlorite–muscovite schist

This schist displays the well-developed schistosity (S2) and is accompanied by recumbent folded S1 quartz veins (Fig. 3b). It is characterized by subhedral garnet porphyroblast, lepidoblastic chlorite and muscovite that define the S2 schistosity (Fig. 4b). The mineral assemblage consists of garnet + chlorite + muscovite + quartz + tourmaline, with minor K-feldspar, ilmenite, magnetite, CM, xenotime, apatite, and zircon. Porphyroblastic garnet (up to 1.3 mm in diameter) contains numerous inclusions of quartz, tourmaline, and CM, which form a curved S0 foliation, with minor xenotime, zircon, and apatite (Fig. 4b). Fine-grained quartz, lepidoblastic chlorite and muscovite

make up the main S2 foliation as well as minor curved S0 foliation in the matrix (Fig. 4b). The orientation of CM produces the darkish flatten cleavages (S1) cutting S0 but following S2 (Fig. 4b). The alignment of S1 CM is partly disturbed by garnet (Fig. 4b). Columnar pleochroic tourmaline in the matrix exhibits brownish core and greenish brown rim with inclusions of CM and follows all foliations from S0 to S2 as a minor component.

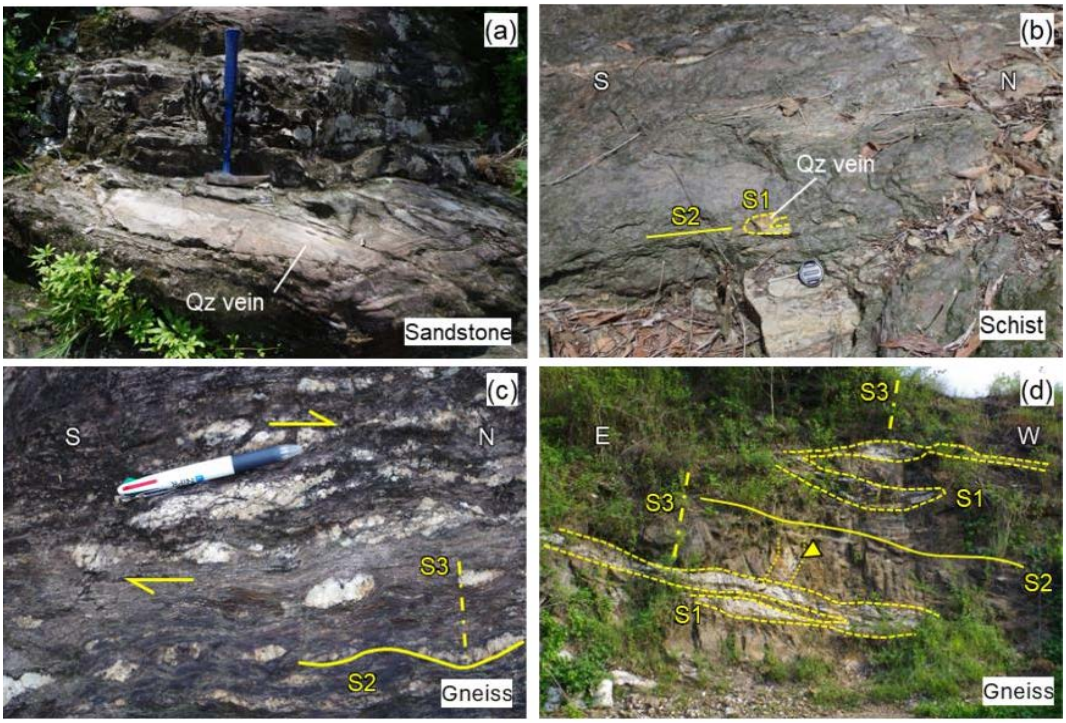

Figure 3. Field occurrences of a sandstone (a) on the north side of study area, schist (b) and gneisses (c, d) on the south side. (a) Bedding plane in a weakly deformed sandstone (82202) is cut by quartz vein. (b) The subhorizontal schistosity (S2) is developed in the schist (82306) and associated with recumbent folded (S1) quartz vein. (c) The mylonitic gneiss (82206) has a subhorizontal foliation (S2) with a sigmoidal leucosome showing top-to-the-north shear sense. The S2 fabric is folded by later upright fold (S3). (d) The subconcordant leucogranite intrusion into a gneiss (82208) is recumbent folded (S1) and mylonitized. Note that a part of the leucogranite cut the horizontal foliation (S2) as marked with a yellow triangle. The leucogranite is refolded weakly by upright fold (S3)

3.3. Garnet–biotite–muscovite gneiss

The micaceous gneiss exhibits a gneissose foliation, accompanied by minor leucocratic veins. Coarse-grained muscovite grains are prominently visible on the foliation plane. This rock predominantly comprises subhedral to euhedral garnet porphyroblasts (up to ~ 2.1 mm in diameter), abundant subhedral lepidoblastic muscovite and biotite, and nematoblastic tourmaline. It also contains subordinate quartz and plagioclase, minor ilmenite, apatite, monazite, and zircon. Garnet shows distinct textural zoning, characterized by a relatively inclusion-rich core and an inclusion-poor rim (Fig. 4c). The inclusions are biotite, quartz, ilmenite, and bluish to brownish tourmaline, whose orientation defines the S0 foliation in the garnet core (Fig. 4c). The preferred orientation of fine- to medium-grained biotite and medium- to

coarse-grained muscovite forms a strong mylonitic foliation (S2) and a minor S1 foliation that is oblique to pre-existing S0 (Fig. 4c). Some S1 biotite and muscovite are truncated by the garnet rim (Fig. 4c). Muscovite appears as a lenticular mica fish including biotite and brownish tourmaline. Tourmaline, which is fine- to coarse-grained (up to 1.9 mm in length) and subhedral to euhedral, follows both S1 and S2 foliations, and displays concentric oscillatory zoning in terms of pleochroic color and inclusions. A light brown inner core and a deep blue outer core enriched in fluid inclusions are overgrown by a brownish inner rim, a dark bluish brown outer rim, and a deeper brownish outermost rim containing inclusions of biotite, ilmenite, quartz, apatite, and zircon.

3.4. Garnet–sillimanite–biotite gneiss

This sample exhibits the well-developed gneissosity (S2), which is wavy due to later upright open folding (S3), showing both migmatitic and mylonitic affinities (Fig. 3c). Pinkish garnet, whitish alkali feldspar, and plagioclase porphyroblasts are visible by the naked eyes (Fig. 3c). Associated boudinaged leucosome is mylonitized and displays sigmoidal geometry with a top-to-the-N shear sense and reworked by upright open fold (Fig. 3c). The gneiss is intruded by a subconcordant leucogranite, which is affected by the horizontal fold (S2) and the later upright open one (S3) (Fig. 3d). Notably, a part of the subconcordant leucogranite cuts the S2 mylonitic foliation of pelitic gneiss (Fig. 3d). The gneiss is composed of garnet, sillimanite, biotite, tourmaline, alkali feldspar, plagioclase and quartz with minor apatite, ilmenite, graphite, monazite, xenotime, and zircon (Figs. 4d-e). Sub- to anhedral garnet porphyroblasts (diameter up to 7.2 mm) contain sillimanite, biotite, quartz, apatite, xenotime, and zircon as inclusions (Fig. 4d). Fine- to medium-grained flaky biotite and prismatic to fibrolitic sillimanite in the matrix exhibit a preferred orientation forming the mylonitic S2 fabric (Figs. 4d-e). Some garnet grains are partly replaced by subhedral brown to greenish biotite and sillimanite, which are oriented along the S2 fabric (Fig. 4e). Plagioclase occurs as a sub- to anhedral grain or as myrmekite partly replacing alkali feldspar, which likely grew perpendicular to the S2 foliation. Brown to greenish brown tourmaline exhibits medium- to coarse-grained, anhedral to subhedral shape, containing fine-grained inclusions of biotite, sillimanite, and xenotime. The tourmaline tends to align parallel to the S2 foliation.

3.5. Mylonitized leucogranite

The intrusive leucogranite contains visible pinkish to reddish garnet, prismatic sillimanite, dark tabular biotite, blocky tourmaline, and rare deep blue dumortierite in a hand specimen. Under the microscope, it is composed mainly of fine- to coarse-grained sub- to anhedral K-feldspar and anhedral quartz, with subordinate plagioclase, garnet, sillimanite, biotite, tourmaline, dumortierite, and accessory apatite and zircon (Figs. 4f-h). A part of K-feldspar is replaced by myrmekite, which is in contact with oriented S2 sillimanite and apparently develops along the S3 cleavage (Fig. 4f). Secondary fine-grained muscovite aggregates are also present along the grain boundary. Subhedral to anhedral garnet often includes abundant tiny inclusions at the center. Sillimanite, biotite, tourmaline, and dumortierite show a preferred orientation along the slightly folded S2 mylonitic foliation (Fig. 4f). The morphology of nematoblastic sillimanite and dumortierite transforms from prismatic at the center into fibrolitic at the margin (Figs. 4f-g). Lepidoblastic brown biotite occurs mainly as a fine-grained flaky aggregate. Tourmaline exhibits a pleochroic color variation, ranging from brown to greenish brown and bluish green. The columnar, bladed

to prismatic dumortierite, identified by its Raman spectra, exhibits strong pleochroism, ranging from ink blue to violet or from pale blue to colorless (Figs. 4g-h). It is in contact with K-feldspar and quartz, and follows the S2 foliation (Fig. 4g).

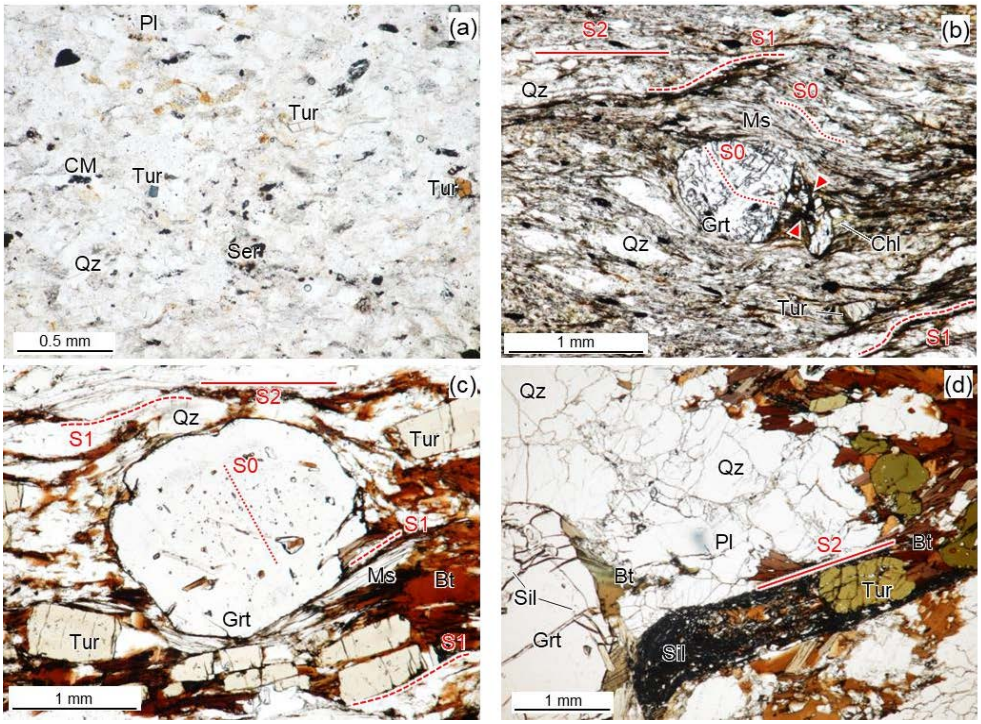

Figure 4. Photomicrographs of sandstone (a), schist (b), muscovite-bearing gneiss (c), sillimanite-bearing gneiss (d, e), and dumortierite-bearing leucocratic granite (f, g), and Raman spectra of dumortierite in leucocratic granite (h). (a) Detrital bluish or brown tourmaline can be seen in weakly deformed sandstone (82202). CM: carbonaceous material. (b) Lepidoblastic fine-grained chlorite and muscovite in the matrix of a schist (82306) define both S0 fabric parallel to the inclusion tails in a garnet and S2 shear fabric forming the schistosity. Carbonaceous materials are condensed along S1 fabric following the axial planar cleavage of the microfold. The S1 fabric is partly disturbed by garnet as indicated with red triangles. (c) The subhedral garnet porphyroblast in a gneiss (82305) has S0 parallel inclusion-rich core and inclusion-poor rim. The oriented biotite, muscovite, tourmaline, and quartz form S1 fabric and S2 shear foliation. Parts of S1 biotite and muscovite are cut by garnet rim. (d) Coarse-grained garnet porphyroblast in a gneiss (82302A) contains sillimanite inclusions in the rim. Biotite, sillimanite, and tourmaline in the matrix display the preferred orientation (S2). (e) Secondary prismatic sillimanite and greenish biotite after garnet orient along the S2 foliation in the gneiss (82302A). (f) Zoned garnet and sillimanite, which is prismatic in the core and fibrolitic in the rim, are present in a leucocratic granite (82204B) intruding into the pelitic gneiss (82204A). The S2 foliation given by oriented sillimanite, biotite, and quartz is folded with a S3 cleavage. A part of K-feldspar is rimmed by myrmekite possibly along the S3 cleavage. (g) Purplish blue dumortierite occurs in the matrix between K-feldspar and quartz in the leucocratic granite (82204B). (h) Raman spectra of analyzed grains fit with that of reference dumortierite (RRUFFID: R060069)

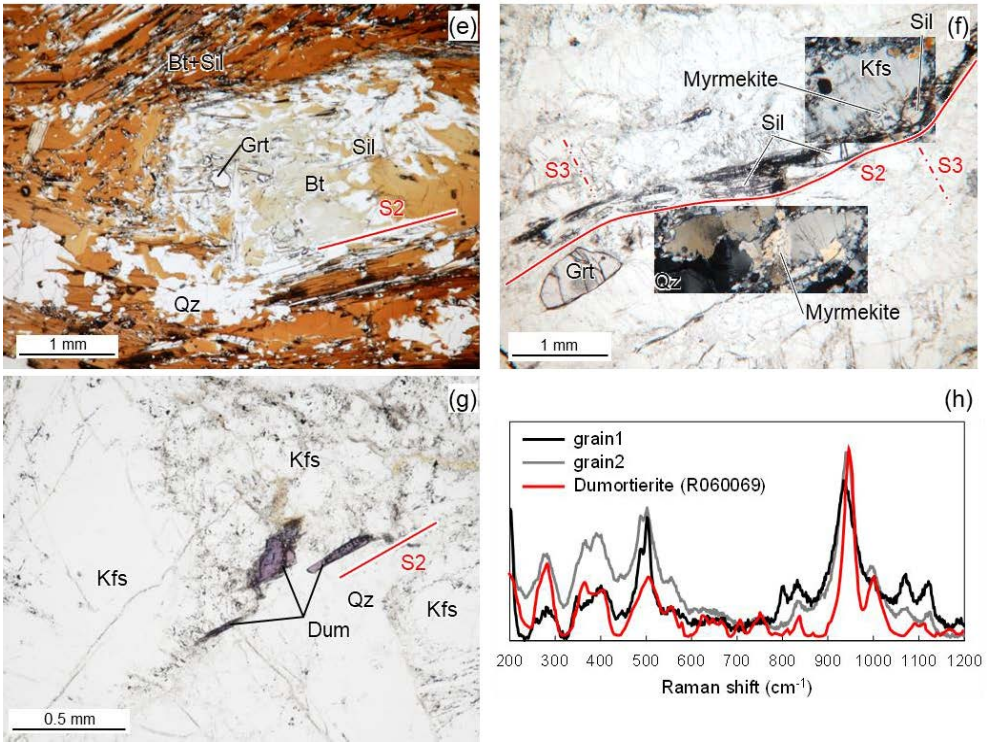

Figure 4. Cont.

4. Analytical methods

A scanning electron microscope equipped with an energy-dispersive X-ray spectroscopy system (JEOL JSM-IT200) at Hokkaido University was used to obtain backscattered electron (BSE) images, which display the detailed occurrence, texture, and chemical zonation of minerals. For the quantitative analysis of constituent minerals in a pelitic gneiss (82204A), for which BSE images had been observed, an electron probe micro-analyzer (EPMA; JEOL JXA-8800R) housed at Hokkaido University was used under operating conditions of 15 kV accelerating voltage, 10 nA beam current, and 2 μm beam diameter. Standards for the analysis were natural minerals and synthetic metals. ZAF correction program was applied for data processing. Representative mineral compositions are shown in Table 1. After confirming the chemical variations of each mineral, some geothermobarometers were applied to estimate the *P*–*T* conditions.

The Raman spectroscopy (HORIBA XploRA PLUS) at Hokkaido University was also utilized to identify sillimanite and dumortierite accurately, and to apply Raman thermobarometry of CM thermometry for a pelitic schist (82306), quartz-in-garnet barometry and zircon-in-garnet thermometry for both the schist (82306) and pelitic gneiss (82204A). Raman spectra of quartz, zircon, and CM inclusions in garnet porphyroblasts were obtained by using an Olympus BX51 confocal microscope equipped with an Olympus 100X objective (NA = 0.9), a 532 nm green laser, and around 2.0 mW irradiation power through a Peltier-cooled CCD camera (256×1024 pixels) under the grading of 1800 lines/mm. Acquisition time was set to 10–15 seconds per spot, with 2–3 integrations per spot. The room temperature was maintained at approximately 22°C. Raman shift calibration was performed using a silicon standard with a Raman peak at

ca. 520 cm^{-1}. The crystal quartz from a pegmatite in Cape Hinode, East Antarctica, and a zircon megacryst from placer deposits in the Central Highlands, Vietnam (Bui et al., 2019) were used as reference standards for each thermobarometry. The CM completely enclosed within garnet was analyzed to avoid mechanical damage during thin section preparation. Following the methodology recommended by Aoya et al. (2010), over 25 CM grains in the pelitic schist were analyzed. The first-order Raman spectra of CM (1000–1800 cm^{-1}) were decomposed into D1-band (~1350 cm^{-1}), D2-band (~1620 cm^{-1}), G-band (~1580 cm^{-1}), and, when present, the minor D3-band (~1500 cm^{-1}) and D4-band (~1200 cm^{-1}). Peak positions, full-width at half-maximum (FWHM), and peak areas of each band were obtained using the Peak Fit 4.12 ver. Program (SeaSolves Software Inc.). All peaks were fitted with a Voigt amplitude function.

Table 1. Representative mineral chemistry

	Grt core	Grt rim	Grt rim margin	fine-Bt in matrix	medium-Bt in matrix	Bt in Grt	Bt in Pl	fine-Pl in matrix	coarse-Pl in matrix	myrmekitic Pl	coarse-Afs in matrix	Sil in Pl	Sil in matrix	Chl
Analysis No.	27	7	2	88	77	22	96	36	115	159	153	110	138	128
SiO_2	37.43	37.29	37.81	37.04	35.62	36.74	36.24	62.69	62.89	61.95	65.48	37.01	37.47	26.39
TiO_2	0.00	0.00	0.00	3.42	2.92	1.60	3.81	0.00	0.00	0.00	0.00	0.00	0.00	0.09
Al_2O_3	21.13	20.97	21.35	20.31	20.17	20.67	19.96	24.28	23.99	23.85	18.91	61.94	62.71	21.41
Cr_2O_3	0.09	0.00	0.01	0.02	0.10	0.05	0.12	0.02	0.00	0.00	0.00	0.06	0.03	0.03
FeO	32.66	32.32	31.94	18.62	18.13	16.48	17.72	0.35	0.00	0.00	0.01	0.12	0.24	26.66
MnO	3.78	2.65	5.85	0.23	0.13	0.00	0.21	0.01	0.00	0.04	0.00	0.04	0.00	0.35
MgO	3.85	4.42	2.63	8.84	8.42	10.30	8.51	0.00	0.00	0.00	0.00	0.03	0.03	13.10
CaO	1.02	1.13	1.10	0.00	0.00	0.06	0.02	5.37	5.13	5.10	0.08	0.02	0.02	0.05
Na_2O	0.01	0.03	0.03	0.11	0.14	0.12	0.12	8.70	8.75	8.62	2.24	0.03	0.03	0.05
K_2O	0.00	0.00	0.01	9.44	9.23	9.23	9.32	0.24	0.57	0.29	13.06	0.00	0.03	0.03
Total	99.96	98.80	100.74	98.04	94.86	95.25	96.03	101.66	101.33	99.84	99.78	99.25	100.56	88.15
Oxgen No.	12	12	12	22	22	22	22	8	8	8	8	5	5	28
Cation														
Si	3.00	3.01	3.02	5.44	5.39	5.47	5.41	2.74	2.76	2.75	2.99	1.01	1.01	5.55
Ti	0.00	0.00	0.00	0.33	0.33	0.18	0.43	0.00	0.00	0.00	0.00	0.00	0.00	0.01
Al	2.00	1.99	2.01	3.53	3.60	3.63	3.51	1.25	1.24	1.25	1.02	1.99	1.99	5.31
Cr	0.01	0.00	0.00	0.00	0.01	0.01	0.01	0.00	0.00	0.00	0.00	0.00	0.00	0.01
Fe	2.19	2.18	2.13	2.32	2.30	2.05	2.21	0.01	0.00	0.00	0.00	0.00	0.01	4.69
Mn	0.26	0.18	0.40	0.02	0.02	0.00	0.03	0.00	0.00	0.00	0.00	0.00	0.00	0.06
Mg	0.46	0.53	0.31	1.94	1.90	2.29	1.89	0.00	0.00	0.00	0.00	0.00	0.00	4.11
Ca	0.09	0.10	0.09	0.00	0.00	0.01	0.00	0.25	0.24	0.24	0.00	0.00	0.00	0.01
Na	0.00	0.00	0.01	0.04	0.04	0.04	0.04	0.74	0.74	0.74	0.20	0.00	0.00	0.02
K	0.00	0.00	0.00	1.76	1.78	1.75	1.77	0.01	0.03	0.02	0.76	0.00	0.00	0.01
Total	8.00	8.00	7.98	15.37	15.38	15.43	15.31	5.01	5.01	5.00	4.98	3.00	3.00	19.79
X_{Mg}	0.17	0.20	0.13	0.46	0.45	0.53	0.46							0.47
X_{Alm}	0.73	0.73	0.73											
X_{Pyr}	0.15	0.18	0.11											
X_{Sps}	0.09	0.06	0.13											
X_{Grs}	0.03	0.03	0.03											
X_{An}								0.25	0.24	0.24	0.00			
X_{Ab}								0.74	0.73	0.74	0.21			
X_{Or}								0.01	0.03	0.02	0.79			

5. Results

5.1. Mineral chemistry

The chemical compositions of garnet, biotite, plagioclase, alkali feldspar, sillimanite, and chlorite in garnet-sillimanite-biotite gneiss (82204A) (Fig. 2) were analyzed by EPMA. This gneiss shares most petrographic characteristics with the same rock type described above. Subhedral garnet porphyroblasts (up to 2.9 mm in diameter) display textural zonation composed of a core enriched in fine- to coarse-grained inclusions of biotite, quartz, apatite, xenotime, and zircon, and an inclusion-poor rim (Fig. 5a). The alignment of biotite and quartz inclusions in garnet core defines the S0 fabric (Fig. 5a). In the matrix, biotite and sillimanite form the main mylonitic foliation (S2) as well as a minor oblique S1 fabric, which is partly cut by garnet rim (Fig. 5a). Alkali feldspar occurs in the matrix either as an anhedral porphyroblast including sillimanite and quartz or as anhedral fine grain, and is partly replaced by myrmekite (Figs. 5b-c). The myrmekite grew perpendicular to the S1 and S2 fabrics (Figs. 5b-c). Secondary chlorite after biotite is present near the myrmekite. Plagioclase also occurs as a sub- to anhedral porphyroblast (up to 4.4 mm in length), containing euhedral biotite and sillimanite, and rounded quartz inclusions (Fig. 5d).

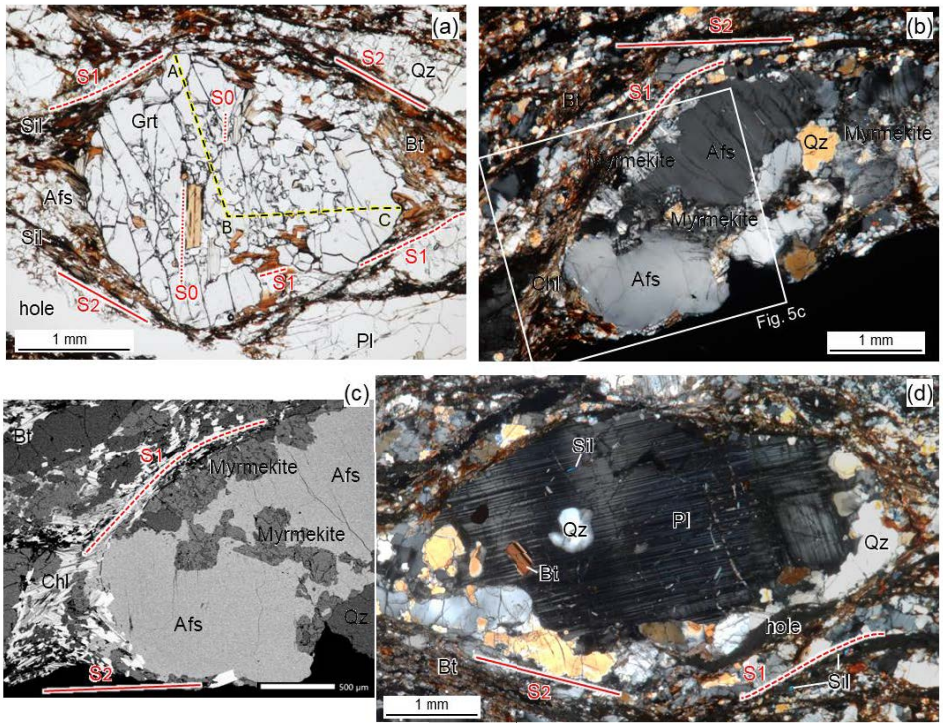

Figure 5. Photomicrographs (a-b, d) and backscattered electron image (c) of a pelitic gneiss (82204A) analyzed for mineral chemistry. (a) Coarse-grained garnet porphyroblast is composed of the core including biotite and quartz with a S0 foliation and inclusion-poor rim truncating likely S1 biotite in the matrix, and wrapped by S2 sillimanite and biotite. Dotted line from A to B to C represents the line profile of chemical analysis. (b) Myrmekite forms around alkali feldspar perpendicular to the S1 and S2 foliations. (c) The backscattered electron image zooming up the area within a white box in (b) shows secondary chlorite after biotite accompanying the myrmekite. (d) Plagioclase porphyroblast contains euhedral sillimanite and biotite and anhedral quartz

The line profile of a garnet porphyroblast shown in Figure 6a indicates nearly constant almandine X_{Alm} [= Fe/(Fe + Mn + Mg + Ca)] and grossular X_{Grs} [= Ca/(Fe + Mn + Mg + Ca)] components within the crystal. However, a decrease in spessartine component X_{Sps} [= Mn/(Fe + Mn + Mg + Ca)] coupled with an increase in pyrope one X_{Pyr} [= Mg/(Fe + Mn + Mg + Ca)] is recognized from the center toward the margin of the garnet. In addition, the garnet margin shows a significant increase in Mn content and a decrease in Mg one (Fig. 6a). The high-Mn and low-Mg domain in the center of garnet is well consistent with its inclusion-rich core (Figs. 5a, 6a). The X_{Mg} [= Mg/(Fe + Mg)] values of garnet, ranging from 0.13 at the margin to 0.22 in the middle portion, are inversely correlated with X_{Sps} (Fig. 6b). The high-X_{Mg} parts correspond to the inclusion-poor rims (Fig. 6a).

Chemical compositions of biotite vary among different occurrences (Fig. 6c). Biotite inclusions in garnet core present high-X_{Mg} values (0.48–0.55) and low-Ti concentrations (0.17–0.22 apfu, based on 22 oxygens). In contrast, those in plagioclase show lower-X_{Mg} values (0.46–0.47) with higher-Ti contents of 0.31–0.43 apfu. Medium-grained biotite in the matrix has a similar composition to the latter with X_{Mg} values of 0.45–0.48 and Ti contents of 0.29–0.38 apfu. On the other hand, X_{Mg} values and Ti contents of the fine-grained one in the matrix are scattered in the ranges of 0.44–0.50 and 0.17–0.38 apfu, respectively.

Plagioclase has mostly homogeneous anorthite contents X_{An} [= Ca/(Ca + Na + K)] of 0.23–0.26, without any correlation with their occurrences (Fig. 6d). However, the orthoclase contents X_{Or} [= K/(Ca + Na + K)] in the core portion of coarse-grained plagioclase that includes sillimanite, biotite, and quartz are slightly higher than other grains (Fig. 6d).

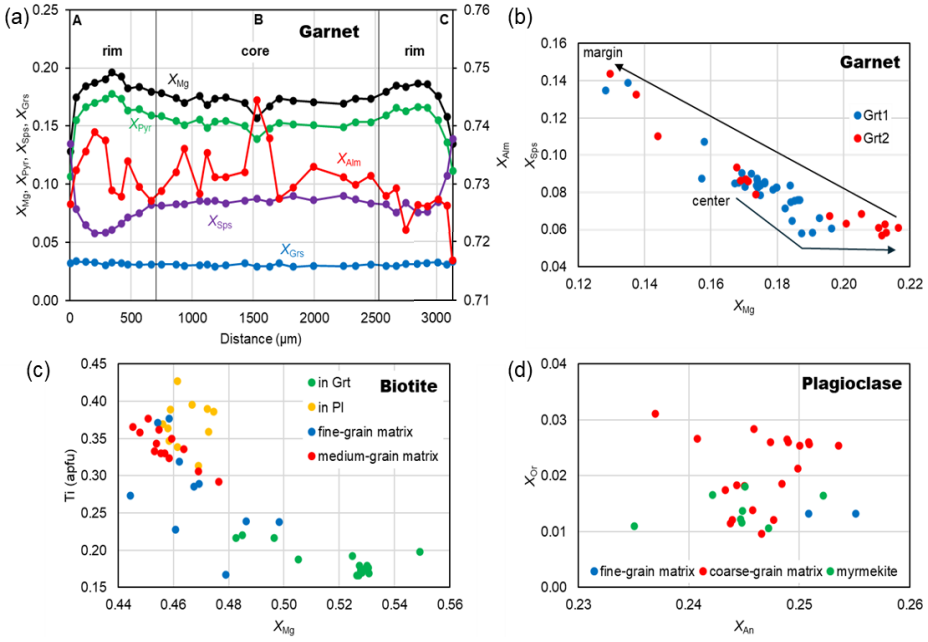

Figure 6. Chemical compositions of garnet (a, b), biotite (c) and plagioclase (d) from a gneiss (82204A) in the sillimanite zone. (a) The line profile of a garnet porphyroblast along dotted line from points A to C shown in Fig. 5a represents the relic prograde zoning modified by retrograde zoning at the margin. (b) X_{Mg} and X_{Sps} values of garnets are negatively correlated. (c) Biotite exhibits chemical variation systematically related with the occurrences. (d) Homogeneous compositions are detected from plagioclase

Alkali feldspar exhibits X_{Or} of 0.79–0.93 with albite contents X_{Ab} [= Na/(Ca + Na + K)] of 0.07–0.21.

Sillimanite crystals in plagioclase have FeO contents of 0.12–0.17 wt%, whereas those in the matrix contain 0.15–0.24 wt%.

Secondary chlorite shows homogeneous X_{Mg} values of 0.45–0.47.

5.2. Raman spectral analysis

We examined the separation between the 205 and 464 cm^{-1} Raman bands (ω1) and between the 128 and 205 cm^{-1} Raman bands (ω2) of a quartz standard and quartz inclusions in garnet from pelitic schist (82306) and gneiss (82204A). The differences of Δω1 = (ω1 of sample) - (ω1 of standard) and Δω2 = (ω2 of sample) - (ω2 of standard) are convertible into the residual pressures (P_{inc}) of quartz in garnet (e.g., Kohn, 2014; Kouketsu et al., 2014). All analytical data were evaluated in terms of the concordance between the pressures at room temperature converted from Δω1 and Δω2, based on Kouketsu et al. (2014). The available data from pelitic schist (82306) showed Δω1 = -1.6–2.6 cm^{-1} (Fig. 7a) and P_{inc} = -0.8–1.4 kbar based on the calculation by Kohn (2014). Those from pelitic gneiss (82204A) presented Δω1 = 0.6–2.0 cm^{-1} and P_{inc} = 0.3–1.0 kbar for quartz inclusions in garnet core and Δω1 = -4.1– -0.1 cm^{-1} and P_{inc} = -2.2–0.0 kbar for those in garnet rim (Fig. 7a).

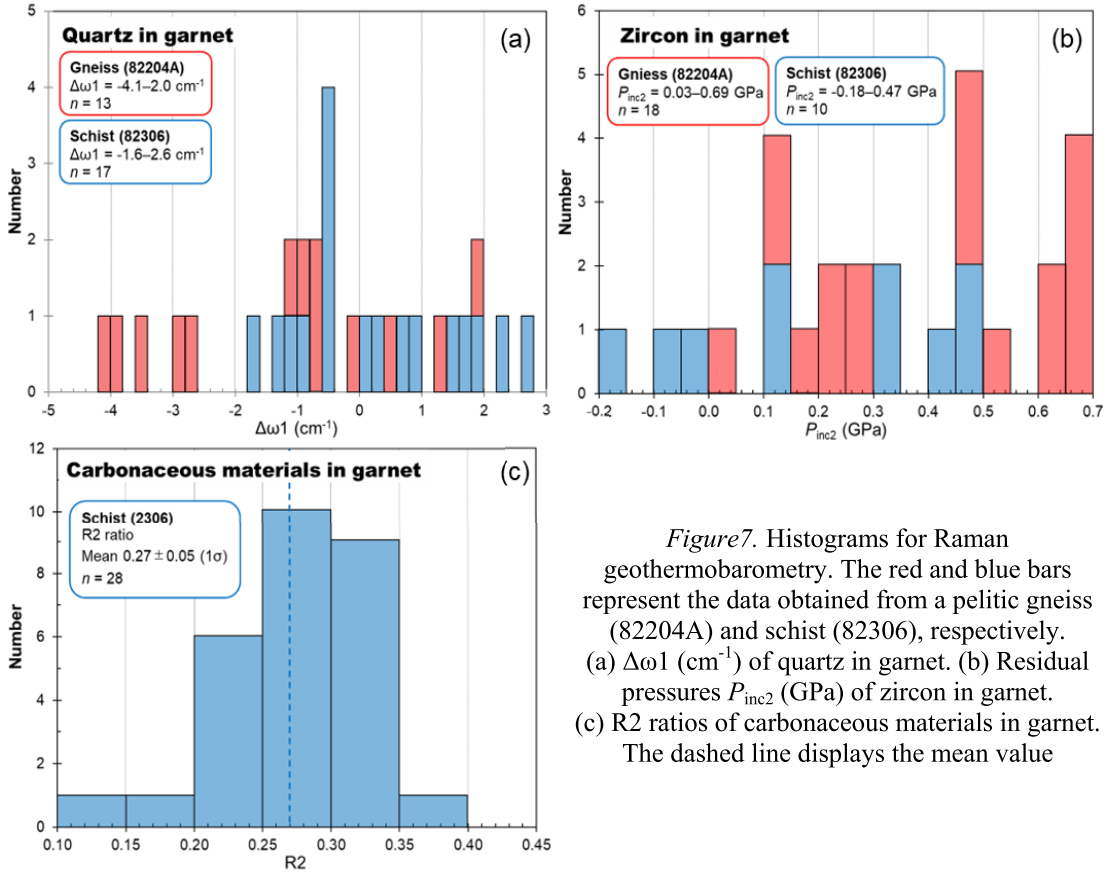

Figure7. Histograms for Raman geothermobarometry. The red and blue bars represent the data obtained from a pelitic gneiss (82204A) and schist (82306), respectively. (a) Δω1 (cm^{-1}) of quartz in garnet. (b) Residual pressures P_{inc2} (GPa) of zircon in garnet. (c) R2 ratios of carbonaceous materials in garnet. The dashed line displays the mean value

Raman spectra of zircon inclusions in garnet from current samples were also analyzed. Zircon generally shows several Raman peaks at *ca.* 202, 214, 224, 356, 439,

975, and 1008 cm^{-1}. The differences of Raman shifts at *ca.* 1008 and 202 cm^{-1} (Δω1), *ca.* 975 and 202 cm^{-1} (Δω2), and *ca.* 439 and 202 cm^{-1} (Δω3) were calculated. Using these factors for both a relaxed zircon standard and zircon inclusions in garnet from analyzed samples, P_{inc1}, P_{inc2} and P_{inc3} derived from Δω1, Δω2, and Δω3 were estimated with following Zhong et al. (2019), respectively. We selected available data that showed good consistency between P_{inc1} and P_{inc2} values, as the approximately 439 cm^{-1} peak converted into P_{inc3} is less sensitive to pressure (Zhong et al., 2019). For the schist (82306), the available P_{inc2} values of 10 zircon inclusions in garnet are scattered between -0.18 and 0.47 GPa (Fig. 7b). Those of 18 zircons in garnet from the gneiss (82204A) show three clusters at 0.03–0.28, 0.46–0.55, and 0.61–0.69 GPa, regardless of textural zonation of garnet (Fig. 7b).

Twenty-eight CM inclusions enclosed in garnet of the schist displayed Raman spectra composed of D1-, G- and D2-bands centered at *ca.* 1336–1366, 1574–1583, and 1602–1628 cm^{-1}, respectively. The FWHM of each band ranges broadly 23–74 cm^{-1} for D1-band, 18–24 cm^{-1} for G-band, and 13–45 cm^{-1} for D2-band (excluding two data points). The mean R2 ratio [= D1/(G + D1 + D2) area ratio] is 0.27 ± 0.05 (1σ) (Fig. 7c).

6. Discussion

6.1. Metamorphic zonation and progressive metamorphism

In the northwestern part of the study area, small outcrops of quartz-rich sandstones were newly found (Figs. 2, 3a, 4a). According to the geological maps by Hoang (1999) and Dinh (2004), the Early Triassic Tan Lac Formation, composed mainly of sandstone and tuffaceous sandstone, is distributed in an N–S trend on the western side of the study area. The northern extension of this formation corresponds to the newly identified outcrops (Fig. 2). Therefore, the lithological and geographical relationships suggest that the sandstone described in this study represents a member of the Tan Lac Formation.

The mineral assemblages of pelitic schists/gneisses indicate the metamorphic zonation of chlorite zone, biotite–muscovite zone, and sillimanite zone, with increasing metamorphic grade toward the east, despite the limited distribution (Fig. 8). The chlorite zone is defined by the occurrence of schists containing mineral assemblages of chlorite + muscovite ± garnet ± biotite. The biotite–muscovite zone is characterized by the appearance of migmatitic and mylonitic gneisses without chlorite that are intruded by a muscovite-bearing deformed leucogranite. Their mineral assemblage consists of garnet, muscovite, and biotite. The sillimanite zone is marked by the presence of sillimanite-bearing and muscovite-free gneisses that are intruded by sillimanite-bearing deformed leucogranite and pegmatite. One leucogranite contains an aluminous borosilicate mineral of dumortierite. These features indicate the successive increase of metamorphic grade from west to east. This metamorphic zonation, displaying the increase of metamorphic grade toward the center of antiformal domed structure, is consistent with previous studies in the DNCV (e.g., Nam et al., 1998) (Fig. 8). The transition from chlorite zone to biotite–muscovite zone, corresponding to the shift from schist to gneiss, is indicative of the reaction where chlorite is consumed to form the biotite + muscovite paragenesis. The reaction isograd could be described as follows:

chlorite + phengitic muscovite + quartz → biotite + muscovite + H_2O

In the sillimanite zone, sillimanite coexists with K-feldspar, while muscovite is absent. These phase relations suggest the consumption of muscovite through the following dehydration melting reactions:

muscovite + quartz → sillimanite + K-feldspar + melt

or muscovite + albite + quartz → sillimanite + K-feldspar + melt

These reactions result in partial melting, which is likely in harmony with the dominance of migmatitic textures and syn-metamorphic leucogranites in the sillimanite zone (Figs. 3c-d), as well as with previous reports (e.g., Nam et al., 1998).

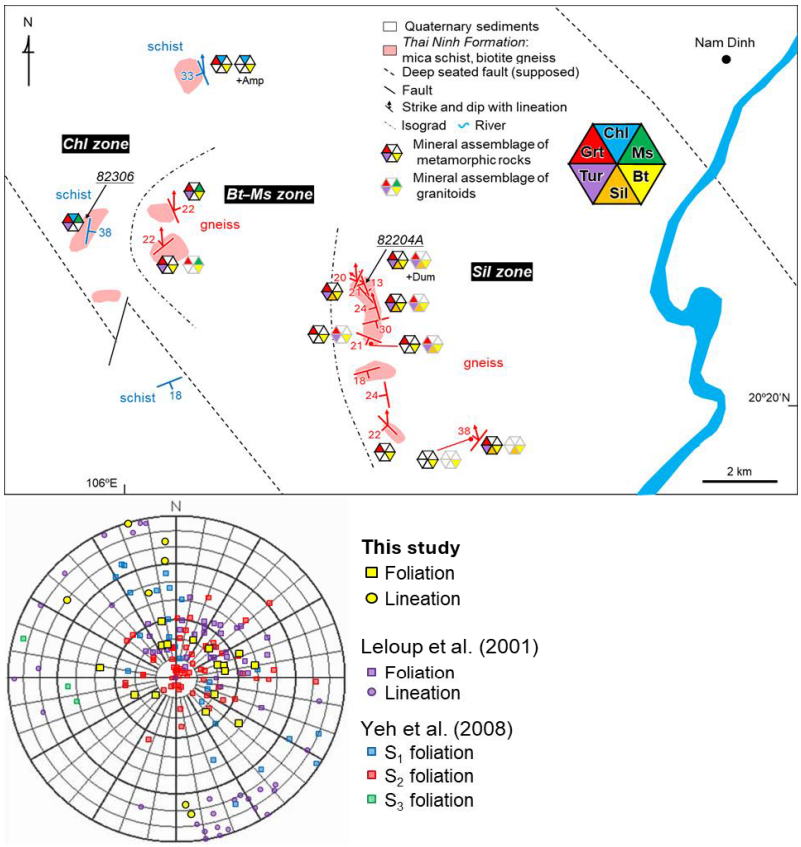

Figure 8. The mineral assemblage and geological structure of metamorphic rocks and granitoids around Nam Dinh. The geological map is same in Fig. 2. The metamorphic zonation composed of chlorite, biotite–muscovite, and sillimanite zones was defined by the parageneses of pelitic schists/gneisses. Various strikes and subhorizontal dips with the shear sense of top-to-the-N to -NW were identified. The structural features are consistent with Leloup et al. (2001) and S2 foliation in Yeh et al. (2008) from same area on the lower hemisphere of Schmidt net

6.2. Pressure–temperature estimation

The *P*–*T* conditions of a garnet–chlorite–muscovite schist from the chlorite zone (82306) and a garnet–sillimanite–biotite gneiss from the sillimanite zone (82204A) were estimated. The conventional geothermobarometry, including garnet–biotite thermometry (Thompson, 1976; Ferry and Spear, 1978; Hodges and Spear, 1982), garnet–chlorite thermometry (Grambling, 1990; Perchuk, 1991), garnet–biotite–plagioclase–quartz barometry (Hoisch, 1990), garnet–aluminosilicate–plagioclase–quartz barometry (Newton and Haselton, 1981; Hodges and Crowley, 1985; Holdaway, 2001), garnet–biotite–aluminosilicate–quartz barometry (Wu, 2017), and two feldspar geothermometer (Stormer, 1975; Stormer and

Whitney, 1985), was applied to the gneiss (82204A).

The peak metamorphic condition was calculated using paired chemical compositions of high-X_{Mg} garnet rim, low-X_{Mg} biotite inclusion in plagioclase, and plagioclase beside the biotite inclusion. The retrograde one was examined using low-X_{Mg} garnet margin, biotite contacting with the garnet margin, coarse-grained plagioclase margin, and secondary chlorite nearby myrmekite in the matrix. Additionally, the temperature condition of myrmekite formation was estimated from a direct contact pair of myrmekite and alkali feldspar. The peak and retrograde metamorphic conditions were obtained at *ca.* 7.0–9.4 kbar and 800–880°C, and 3.0–4.3 kbar and 570–600°C, respectively (Fig. 9a). The peak granulite-facies condition falls on the stability fields of sillimanite + K-feldspar + melt and biotite + sillimanite + K-feldspar + quartz + melt (Fig. 9a), consistent with aforementioned petrographic descriptions. This condition is also equivalent to the limit of the dumortierite stability condition (Fig. 9a). Dumortierite was discovered from a leucocratic granite subconcordantly intruding into the gneiss in the sillimanite zone (Figs. 4g-h). This leucogranite contains garnet + sillimanite + biotite + K-feldspar assemblage, similar to the host gneiss (Figs. 4f-h, 8). The field occurrence and petrography of the granite imply that it is syn-metamorphic and may have coexisted with the host gneiss at peak granulite-facies condition. Thus, it is inferred that dumortierite in the syn-metamorphic granite was stable at the peak condition. This constrains the peak metamorphic condition of the gneiss accompanied by leucogranite to approximately 7.0–8.5 kbar and 800–830°C (Fig. 9a).

The retrograde condition across the stability fields of andalusite and sillimanite is consistent with the absence of andalusite after sillimanite in the analyzed gneiss and leucogranite (Figs. 4d-f, 5). Furthermore, the lack of secondary muscovite and cordierite in the analyzed gneiss indicates a retrograde path within the stability field of sillimanite + K-feldspar + biotite + quartz + melt, as illustrated in Fig. 9a. However, according to the petrogenetic grids, before reaching the above retrograde condition, reactions consuming sillimanite + K-feldspar + melt are likely to happen during cooling under the H_2O-saturated suprasolidus condition (Fig. 9a). It is possible that the melt coexisting with the gneiss was H_2O-undersaturated under the low-X_{H2O} environment during the retrograde stage. The low-X_{H2O} in the melt raises the solidus temperature (Le Breton and Thompson, 1988). It shifts the above reactions producing muscovite + quartz to lower temperature (e.g., Holdaway and Lee, 1977) (Fig. 9a). The presence of graphite in the gneiss may have reduced the water activity of coexisting melts. Such low-X_{H2O} in melts probably allows the current gneiss to reach the retrograde condition without reactions producing secondary muscovite after sillimanite + K-feldspar. It is consistent with Leloup et al. (2001), who assumed low-X_{H2O} = 0.3–0.5 due to CO_2-rich fluid activity during HT metamorphism. Myrmekite replacing alkali feldspar in contact with sillimanite likely formed between *ca.* 550–610°C at 4 kbar, similar to the retrograde metamorphic condition calculated above (Fig. 9a). Such myrmekite growth around K-feldspar porphyroclasts is generally considered to indicate the HT deformation at *ca.* 550–650°C (Passchier and Trouw, 2005; Chen et al., 2023 and references therein), and has been reported from the mylonites in both the DNCV (Dinh et al., 2023) and the RRSZ (e.g., Chen et al., 2023).

Raman thermobarometry using quartz (Kohn, 2014; Kouketsu et al., 2014), zircon (Zhong et al., 2019), and CM inclusions (e.g., Aoya et al., 2010) in garnet provides a powerful tool for estimating metamorphic conditions independently of the above

conventional geothermobarometers. Quartz-in-garnet Raman barometry was applied to quartz inclusions in garnet core of pelitic gneiss, which exhibit Raman spectral features with $\Delta\omega1$ = 0.6–2.0 cm^{-1} and P_{inc} = 0.3–1.0 kbar (Fig. 7a). In combination with garnet–biotite thermometer using garnet core and its biotite inclusion, the prograde metamorphism that formed the garnet core might have occurred at *ca.* 7.5–9.5 kbar and 610–650°C (Fig. 9b). The range of residual pressures preserved in quartz in garnet rim ($\Delta\omega1$ = -4.1—0.1 cm^{-1} and P_{inc} = -2.2–0.0 kbar) (Fig. 7a) possibly reflects the entrapment of some α-quartz with various residual pressures during garnet rim growth at the pre-peak stage. This possibly indicates the *P–T* change across contour lines of α-quartz residual pressures in Kohn (2014) between -2 and 0, from the prograde to peak metamorphic conditions (Fig. 9b). Zircon inclusions in the garnet gave a broad range of residual pressures, which are strongly dependent on temperature (Zhong et al., 2019), and separated into three distinct clusters at 0.03–0.28, 0.46–0.55, and 0.61–0.69 GPa without apparent correlation to garnet textural zonation (Fig. 7b). Zircon with low residual pressures of 0.03–0.28 GPa close to zero, obviously reflects the relaxation that released the residual pressures as Zhong et al. (2019) reported. The higher residual pressures of 0.46–0.55 and 0.61–0.69 GPa in zircon are expected to retain the temperature conditions when the zircon was trapped in garnet. The average residual pressure values of 0.50 and 0.66 GPa with the inherited error of 0.035 GPa for this barometer, yield temperature ranges of *ca.* 620 to 700°C and 860 to >900°C at 9 kbar, respectively, by assuming almandine garnet for the host (Fig. 9b). These are almost in agreement with the *P–T* ranges inferred from conventional geothermobarometry for garnet core and rim formation (Fig. 9b). Nevertheless, they gave slightly higher temperature conditions, especially for high-Mg garnet rim, possibly due to the effect of pyrope components in garnet. Zhong et al. (2019) demonstrated that entrapment temperatures can differ by up to 200°C at 10 kbar between zircon in garnet with almandine80–pyrope20 and almandine60–pyrope40 components.

In the pelitic schist (82306), the clustered R2 ratios of 28 CM grains (Fig. 7c) provided the metamorphic temperature of 515±27°C, consistent with the stability field of garnet + chlorite + muscovite paragenesis in this schist (Figs. 4b, 8, 9b-c). Quartz inclusions in garnet, showing $\Delta\omega1$ = -1.6–2.6 cm^{-1} (Fig. 7a) and P_{inc} = -0.8–1.4 kbar, might preserve a broad range of entrapment pressure conditions between *ca.* 4.0 and 7.5 kbar at 500°C. Alternatively, except for the quartz with the maximum frequency shift, which plausibly preserves the residual pressure reflecting the near-peak metamorphic condition (Kouketsu et al., 2014), residual pressures of other inclusions were modified through invisible microcracking. However, their $\Delta\omega1$ values are relatively clustered around 2.0 and -0.5 cm^{-1} (Fig. 7a). This suggests that these values are meaningful for constraining pressure conditions, as discussed later. Zircon inclusions in garnet showed scattered residual pressures between -0.18 and 0.47 GPa, which can be roughly divided into a lower group at -0.18–0.13 GPa and a higher one at 0.31–0.47 GPa (Fig. 7b). The former is possibly attributed to the relaxation effect of the zircon inclusions. The mean value of the residual pressures of the latter is approximately 0.40 GPa, which is consistent with the temperature condition obtained from the CM Raman geothermometer (Fig. 9b), despite a somewhat broad range. These results suggest that the garnet grains in this schist have grown during a near-isothermal pressure change (Fig. 9b).

6.3. Structural correlation with regional deformation events and metamorphic stages

The relationship between the microstructures and main constituent minerals observed in metamorphic rocks in the study area is summarized in Table 2. The

main foliations (S2) of schists and gneisses in this study exhibit various strikes and gentle dips, with the lineation showing top-to-the-N to -NW shear sense (Fig. 8). The structural features are comparable with those stated by Leloup et al. (2001) and Yeh et al. (2008) (Fig. 8) and correspond to the dominant metamorphic fabrics of large-scale horizontal D2 folds formed by vertical shortening in the DNCV (Yeh et al., 2008), as observed in some outcrops (Figs. 3b-d). The penetrative subhorizontal S2 foliation associated with mylonitization is also preserved in leucosome and leucogranite (Figs. 3c-d, 4f-g) and wraps garnet porphyroblasts in schists and gneisses (Figs. 4b-e, 5, Table 2). Secondary subhedral biotite and sillimanite after anhedral garnet in pelitic gneiss, which obviously indicates a back reaction of garnet with anatectic melt during the retrograde stage, follow the S2 foliation (Fig. 4e, Table 2). Taking local intrusion of leucogranite cutting the S2 foliation (Fig. 3d) into account, the D_2 deformation event should have happened under the post-peak suprasolidus condition.

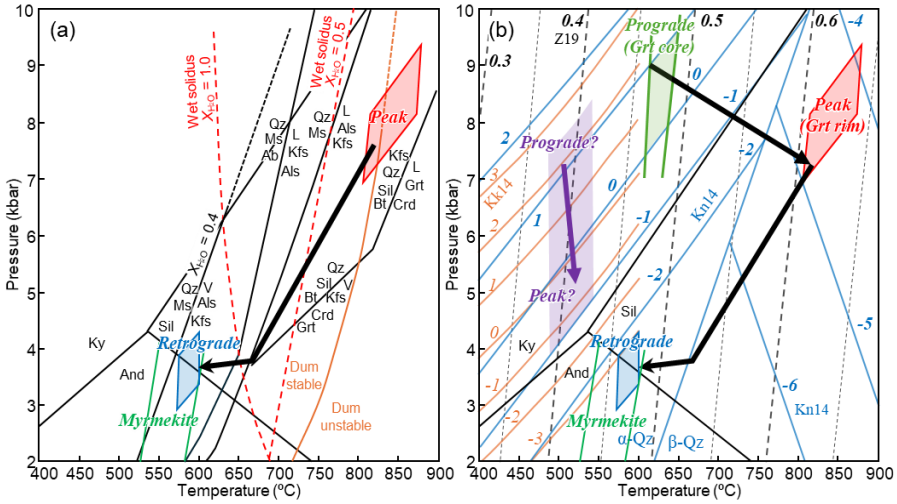

Figure 9. P–T estimates of a pelitic schist (82306) in the chlorite (Chl) zone and gneiss (82204A) in the sillimanite (Sil) zone. The light green, red, blue, and green boxes represent the prograde, peak, retrograde, and myrmekite formation conditions of the pelitic gneiss (82204A), respectively, with an inferred *P–T* path shown with a thick black arrow. The pale purple box shows the metamorphic condition for the schist (82306) with a thick purple arrow showing a speculative *P–T* path. (a) Results of conventional geothermobarometers. The melting reactions involving muscovite (Ms) and aluminosilicate stability fields are referred from Spear et al. (1999). The reactions accompanied with Sil and biotite (Bt), Ms + quartz (Qz) at X_{H2O} = 0.4 and dumortierite stability curve are after Kriegsman and Hensen (1998), Holdaway and Lee (1977), and Ranaweera et al. (2007), respectively. Wet solidi at X_{H2O} = 0.5 and 1.0 with red dashed lines are from Le Breton and Thompson (1988). (b) Results of Raman geothermobarometers. The contour lines of $\Delta\omega 1$ (cm^{-1}) and residual pressures (kbar) of Qz in garnet (Grt) (Kohn, 2014: Kn14; Kouketsu et al., 2014: Kk14), and residual pressures (GPa) of zircon in Grt (Zhong et al., 2019: Z19) are drawn in orange, blue, and black, respectively. (c) Combination metamorphic fabrics of S0–S2 with a *P–T* path. The reaction related with Grt + Chl + Ms is after Spear and Cheney (1989). (d) Reported *P–T* paths (Nam et al., 1998; Leloup et al., 2001; Palin et al., 2013) and conditions (Nam et al., 1998; Leloup et al., 2001; Gilley et al., 2003; Anczkiewicz et al., 2007; Palin et al., 2013) from the Day Nui Con Voi metamorphic complex (DNCV) are present with thick dark gray dashed arrows and the light gray ellipses and boxes, respectively. The dark gray box and star marks indicate *P–T* conditions of the Bu Khang Dome (BKD) (Jolivet et al., 1999, 2001). The *P–T* paths of the northern and central Red River Shear Zone (RRSZ) reported by Leloup et al. (1995, 2001) were also shown with white arrows

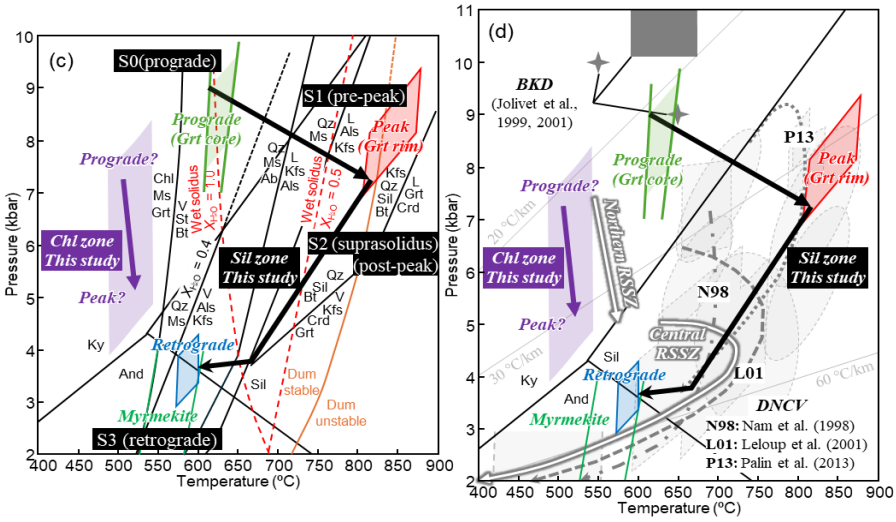

Figure 9. Cont.

Table 2. Summary of microstructures and main constituent minerals

Zone	*Chl zone*		*Bt–Ms zone*		*Sil zone*				
Sample	Grt–Chl–Ms schist (82306)		Grt–Bt–Ms gneiss (82305)		Grt–Sil–Bt gneiss (82302A)		Grt–Sil–Bt gneiss (82204A)		luecogranite (82204B)
	main minerals	*relation with Grt*	main minerals	*relation with Grt*	main minerals	*relation with Grt*	main minerals	*relation with Grt*	main minerals
S0	Qz+CM in Grt Ms+Chl in the matrix	*in Grt*	Qz+Bt+Ilm in Grt	*in Grt core*			Bt+Qz in Grt	*in Grt core*	
S1	CM in the matrix	*cutting by Grt*	Bt+Ms+Tur in the matrix	*cutting by Grt rim*			Bt+Sil+Qz in the matrix	*cutting by Grt rim*	
S2	Ms+Chl+Qz in the matrix	*wrapping Grt*	Bt+Ms+Tur in the matrix	*wrapping Grt rim*	Bt+Sil+Tur in the matrix 2nd Bt+Sil after Grt in the matrix	*wrapping Grt rim* *replacing Grt*	Bt+Sil+Qz in the matrix	*wrapping Grt rim*	Bt+Sil+Dum+Qz in the matrix
S3					Myrmekite after Kfs? in the matrix		Myrmekite after Afs? 2nd Chl after Bt? in the matrix		Myrmekite after Kfs? in the matrix

The subhorizontal S2 foliation is refolded by open upright folds (Figs. 3c-d, 4f), which could be equivalent to the D_3 upright folds during a doming event and simultaneous exhumation with crustal strike-slip shearing of the RRSZ (e.g., Yeh et al., 2008; Dinh et al., 2023). Myrmekite after K-feldspar formed vertical to the S1 and S2 foliations and likely parallel to the S3 cleavage of the upright fold occasionally in contact with chlorite and sillimanite (Figs. 4f, 5b-c, Table 2). Thus, this texture might be post-D_2 formation, possibly related to fluid infiltration during the D_3 event.

In addition, the S0 and S1 foliations before the S2 are preserved in garnet core and matrix, respectively (Figs. 4b-c, 5, Table 2). The S1 fabric is apparently interrupted by the garnet rim (Figs. 4b-c, 5a, Table 2). These textures may indicate the S0 and S1 foliations developed before or during the garnet core growth and before the garnet rim growth, respectively. Previous studies have reported

that the HT D1 upright fold is formed by horizontal shortening of pre-existing metamorphic layering (Yeh et al., 2008; Dinh et al., 2023). As the oblique intersection between S0 and S1 (Figs. 4b-c, 5a), it might result in pre-existing S0 foliation being folded by D_1 upright fold with S1 cleavage during prograde metamorphism. The alignment of prismatic sillimanite along with the S1 fabric in pelitic gneiss (Figs. 5a, d) indicates the D_1 event might have occurred under the sillimanite stability condition during the prograde stage.

Consequently, the gneiss in the sillimanite zone of study area recorded a clockwise *P–T* path with peak granulite-facies condition (Fig. 9c). Garnet core grew during the prograde metamorphism associated with S0 foliation. This was followed by progressive heating and D_1 upright folding, accompanied by sillimanite formation during the pre-peak stage. The gneiss gained the peak granulite-facies condition associated with garnet rim growth and low-X_{H2O} anatexis melt. Subsequently, D_2 subhorizontal folding and mylonitization occurred under post-peak suprasolidus condition during uplifting. Finally, myrmekite formed after alkali feldspar porphyroclasts through fluid activity, possibly related with D_3 doming event, under the subsolidus retrograde condition on sillimanite-andalusite reaction line (Fig. 9c). The correlation between metamorphic stages and ductile deformation history is almost concordant with that of the DNCV proposed by Dinh et al. (2023).

Schist in the chlorite zone exhibits similar structural features to those of gneisses in the sillimanite zone (Figs. 2b, 3b, 8), which implies that both underwent the same metamorphic–deformation process with a clockwise *P–T* path. Relative bimodal $\Delta\omega1$ values of quartz inclusions in garnet at *ca.* 2.0 and -0.5 cm^{-1} (Fig. 7a) and near-constant temperature (Fig. 7c) for garnet crystallization were detected from the schist. These results likely indicate garnet growth while preserving the S0 fabric during near-isothermal decompression from approximately 7.5 kbar (prograde stage) to approximately 5 kbar (peak stage) at 515±27°C, accompanied by a clockwise *P–T* change (Figs. 9b-c).

The *P–T* path and metamorphic conditions of the gneiss in the sillimanite zone are also well comparable with those reported from not only the DNCV but also central RRSZ (Fig. 9d), despite slight differences from peak metamorphic conditions documented in Nam et al. (1998) and Leloup et al. (1995, 2001). The schist in the chlorite zone has a *P–T* path which resembles the northern RRSZ reported by Leloup et al. (1995, 2001) (Fig. 9d). Although the prograde metamorphic condition of the gneiss and metamorphic condition of a low-grade schist in the chlorite zone presented in this study are the first reports in the DNCV, the current pelitic schists and gneisses in Nam Dinh have lithological, petrological and structural characteristics similar to those of the DNCV. Their similarity strongly suggests the metamorphic rocks in Nam Dinh represent the southeastern extension of the DNCV. The above comparison allows us to reconstruct the geothermal gradients of 20–25°C/km at the prograde stage, *ca.* 30°C/km at the peak stage, and *ca.* 60°C/km during the retrograde stage in the DNCV (Fig. 9d). The geotherms from the peak stage to retrograde stage in this study are in harmony with previous report from the DNCV by Leloup et al. (2001).

6.4. Regional tectonothermal history and tectonic implications

In the DNCV, the exhumation process of the metamorphic rocks has been well discussed by numerous studies mainly based on the K–Ar/Ar–Ar geochronology which reflects cooling history due to the low-closure temperature of *ca.* 300–500°C (Nam et al., 1998; Wang et al., 1998, 2000; Leloup et al.,

2001; Garnier et al., 2002; Gilley et al., 2003; Anczkiewicz et al., 2007; Yeh et al., 2008; Dinh et al., 2023 and references therein). The Cenozoic sinistral shearing along the RSSZ played a crucial role in the uplift of these high-grade metamorphic rocks, as follows. Nam et al. (1998) proposed that exhumation of the DNCV was triggered by the coeval sinistral strike-slip displacement of the RSSZ during *ca.* 31–24 Ma. The rapid cooling process, spanning approximately 27 to 17 Ma, was identified across the entire RSSZ, and the diachronous propagation of left-lateral movement from southeast to northwest was suggested (Wang et al., 1998, 2000). Leloup et al. (2001) proposed the activation of the RSSZ sharing since *ca.* 35 Ma during HT metamorphism (T >700°C). They explained the mechanism of cooling diachronism along the RSSZ by zipper tectonics, with a progressive clockwise rotation of the Indochina Block during left-lateral strike-slip shearing. However, a rapid cooling path without diachronism was detected in the DNCV between approximately 28 and 23 Million Years Ago. Further antiformal doming of the DNCV, concurrent with the shearing of the RSSZ, promoted vertical uplift accompanied by rapid denudation and normal fault activities during approximately 26–22 Ma (Anczkiewicz et al., 2007; Yeh et al., 2008; Dinh et al., 2023). On the other hand, the driving force for producing granulite- to upper amphibolite-facies metamorphic rocks in the DNCV has been poorly discussed. Leloup et al. (2001) proposed the shear heating by left-lateral shear along the RSSZ to generate the high-thermal gradient. Whereas Gilley et al. (2003) pointed out that the heat production caused by shearing was insufficient, they alternatively attributed the HT metamorphism to hot magma ascending (Gilley et al., 2003; Anczkiewicz et al., 2007).

As introduced above, the timing of the left-lateral shearing of the RSSZ has been controversial, possibly due to the traditional basis of K–Ar/Ar–Ar dating. The dating methodology exhibits some caution regarding age reliability due to the less durable nature of host minerals, such as micas, the high mobility of K and Ar through fluid infiltration or thermal events, even at temperatures below 300°C, and the presence of excess Ar. While, zircon U–Pb and monazite U–Th–Pb dating is known to produce precisely metamorphic ages during HT metamorphism owing to high-closure temperatures over 700°C, physical and chemical durability of zircon and monazite. Thus, based on previous geochronological reports especially utilizing these dating, the timeline of the thermal history can be summarized as follows: peak granulite-facies metamorphism at *ca.* 38–34 Ma (Palins et al., 2013), the initiation of strike-slip shearing along the RRSZ after *ca.* 31 Ma (Palins et al., 2013) and possibly at 27.5 Ma (Wang et al., 2000), ductile deformation ceased at *ca.* 25 Ma (Palins et al., 2013), and further cooling and uplifting until around 20 Ma (Wang et al., 1998, 2000; Leloup et al., 2001; Garnier et al., 2002; Gilley et al., 2003; Dinh et al., 2023). Occurrences of the Eocene (*ca.* 37 Ma) granitic mylonite and Oligocene (*ca.* 31–29 Ma) syn-kinematic granitic dyke with ductile shearing fabric were identified from the northern extension of the DNCV (Chen et al., 2019). The former is thought to be correlated with high-potassium alkaline magmatic activity during the Eocene to Oligocene (*ca.* 43–30 Ma) in an extensional post-collisional setting along the RRSZ, and the latter was derived from anatectic melts of the lower crust during ductile shearing (Chen et al., 2019, and references therein). The contemporaneity between granulite-facies metamorphism and extensional alkaline magmatism at Eocene indicates the magmatism can be a candidate for the heat source driving granulite-facies metamorphism in the DNCV. Some previous studies have

proposed that advective hot magmatism, such as upwelling asthenosphere, is the mechanism that produces the granulite-facies HT condition for the DNCV (e.g., Gilley et al., 2003; Anczkiewicz et al., 2007). Furthermore, the timing of the post-peak D_2 subhorizontal folding with anatectic melts may be constrained at *ca.* 31–29 Ma, based on the reported ages of syn-kinematic granitic dykes (Chen et al., 2019) and their occurrences recognized in this study (Fig. 3d). Strike-slip shearing along the RRSZ was possibly activated between *ca.* 27–25 Ma in the DNCV, accompanied by the D_3 antiformal doming and probably myrmekite formation (Figs. 4f, 5b-c) under the lower amphibolite- to greenschist-facies condition. This speculation aligns well with the tectonothermal history of the DNCV proposed by Dinh et al. (2023).

In northern Vietnam, the Oligocene–Eocene thermal and/or exhumation tectonics are recorded not only in the DNCV but also in the Song Chay massif, Phan Si Pan zone, and Bu Khang Dome (BKD) (e.g., Jolivet et al., 2001; Anczkiewicz et al., 2007) (Fig. 1b). The Song Chay massif is a broad orthogneiss antiformal dome trending NE–SW and composed mainly of migmatites, granitoids, and augen gneisses. These rocks originated from Ordovician–Silurian granitic magmatism and underwent possibly Silurian metamorphism, as well as the Triassic Indosinian orogeny (Roger et al., 2000; Jolivet et al., 2001; Maluski et al., 2001; Gilley et al., 2003; Travin et al., 2024, and references therein). The orthogneisses also record local thermal heating by Jurassic to Cretaceous granitoid intrusions and rapid cooling during the 28–20 Ma period, resulting from sinistral strike-slip shearing along the RRSZ (Maluski et al., 2001; Travin et al., 2024). The Phan Si Pan zone is a NW–SE trending large granitoid complex that experienced multiple magma pulses during the Archean, Paleoproterozoic, Neoproterozoic, Permian, and Cenozoic periods (Pham et al., 2020, and references therein). The last Cenozoic magmatism produced A_1-type alkaline granite derived from an enriched mantle with within-plate affinity at *ca.* 52–49 Ma, granodiorite to syeno-diorite generated from the mixture of the mantle source and lower crustal anatectic melts caused by mantle upwelling at *ca.* 35–34 Ma, and subsequent calc-alkaline peraluminous leucogranite derived from crustal melting in the tensional or post-collisional regime at *ca.* 35–31 Ma (Pham et al., 2020). Such mantle-derived alkaline magmatism, contemporaneous with crust-melted leucogranitoid magmatism between approximately 40 and 30 Ma, has been confirmed along or around the RSSZ, including the Phan Si Pan zone (e.g., Chung et al., 1997; Zhang and Schiirer, 1999).

The BKD is a Cenozoic metamorphic core complex that forms an antiformal dome with a WNW–SES trending axis. It consists of micaschists (kyanite- and staurolite-bearing garnet–biotite–phengite metapelite, two mica sillimanite schist), paragneisses (biotite–sillimanite gneiss), orthogneisses, and intrusive granitoids (Jolivet et al., 1999, 2001; Nagy et al., 2000; Garnier et al., 2002). The core complex is overlain by a marble and metabauxite unit, as well as Mesozoic sedimentary rocks, via detachment faults. Metamorphic conditions recorded in the micaschists reached pressures greater than 9 kbar and temperatures of 550±50°C, with biotite/muscovite K‑Ar ages of approximately 27–21 Ma, which are considered to be the timing of exhumation and extensional shearing (Jolivet et al., 1999; Garnier et al., 2002). Two gneissose granitoids in the BKD showed U–Pb ages of *ca.* 26–24 Ma by dilution methods for monazite, zircon, and allanite, Rb–Sr isochron ages of *ca.* 21–20 Ma using biotite and K-feldspar fractions, Sr–Nd isotopic compositions representing a mixture of evolved crust and mantle-derived magmas

(Nagy et al., 2000). Jolivet et al. (2001) highlighted the similarity between the DNCV and BKD in terms of the HT subhorizontal ductile deformation and exhumation process associated with dome formation, which occurs through extensional shearing of the RRSZ, although no kyanite has been reported from the DNCV. They suggested that the India-Asia collision during the Eocene resulted in crustal thickening, leading to kyanite-grade metamorphism in the BKD. The BKD metamorphic rocks also underwent a transition from a compressional to an extensional regime through the extrusion of a thickened crust into the extensional region or the correlation with the onset of East Sea rifting (Jolivet et al., 2001). Furthermore, the granitoids in the BKD are likely to have been generated by upwelling mantle-derived magma due to the extensional lithospheric thinning (Nagy et al., 2000).

As for the metamorphic conditions, the kyanite-grade metamorphic condition of the BKD is apparently comparable with the prograde one of the sillimanite-grade gneiss in the DNCV, which is newly identified in this study (Fig. 9d). The regional kyanite-grade Himalayan metamorphism took place at *ca.* 8–12 kbar and 620–720°C during *ca.* 45–30 Ma along the Greater Himalayan metamorphic Sequence in Nepal (Searle and Cottle, 2024, and references therein). These conditions are in harmony with the kyanite-grade *P–T* conditions of the DNCV and BKD (Fig. 9d). Therefore, the DNCV might have experienced the crustal thickening caused by the Himalayan orogeny during the prograde stage, which could have produced the S0 and S1 foliations with D_1 upright folding through the crustal thickening. Subsequently, extensional mantle-derived magmatism with crustal thinning happened not only in the DNCV but also the BKD and the Phan Si Pan zone, and let the DNCV reach the peak granulite-facies condition with anatexis (Figs. 9c-d). Consequently, the DNCV, BKD, and Phan Si Pan zone likely share a similar tectonothermal history from the Eocene to Oligocene and were uplifted together with the Song Chay massif during the Early Miocene.

The left-lateral shearing and doming uplifting, along with extrusion tectonics of the RRSZ, including the DNCV, have been considered to be initimated with the East Sea opening (e.g., Tapponnier et al., 1982). According to previous studies (e.g., Mai et al., 2018), the East Sea initiated its initial seafloor spreading in the northern part approximately 32 Ma, following the back-arc magmatism that occurred at 40 Ma, due to the northward subduction of the Neotethys Ocean. This was followed by the southward ridge jump at *ca.* 23 Ma and termination of the opening at *ca.* 15 Ma (Mai et al., 2018; Dinh et al., 2023, and references therein). Dinh et al. (2023) proposed a thermal evolution model for the DNCV, taking into account the India–Asia collision and the East Sea opening. The collision resulted in crustal thickening, accompanied by horizontal shortening and upright folding (D1), under granulite to upper amphibolite-facies conditions before 32 Ma. Subsequent horizontal to subhorizontal folding (D_2) was led by the collapse of the thickened crust due to the crustal thinning attributed to back-arc extension for the opening of the East Sea at amphibolite-facies conditions between 32 and 26 Ma. The greenschist-facies doming event (D_3) occurred not through the synchronous left-lateral shearing of the RRSZ, but rather through rapid tropical denudation between approximately 26 and 22 Ma. Additionally, the left-lateral shearing triggered both the southeastward extrusion tectonics of the Indochina Block and the southward ridge jump of the East Sea.

Based on our results and interpretation summarized in Table 3, the D1 event related to the India-Asia collision and characterized

by a geothermal gradient of 20–25°C/km probably occurred during the pre-peak prograde stage before the Late Eocene. The peak granulite-facies metamorphism associated with crustal anatexis at a 30°C/km geotherm could be attributed to extensional magmatism in the Late Eocene, which is coeval with the initial back-arc magmatism and crustal thinning before the opening of the East Sea (Table 3). The extensional–accretionary setting, such as the back-arc extension, is well known for explaining short-lived granulite-facies metamorphism (less than 5–10 Myr at temperatures exceeding 800°C) correlated with coeval magmatism (e.g., Harley, 2016). Although the duration of the granulite-facies metamorphism in the DNCV remains obscure, the post-peak rapid cooling process (e.g., Nam et al., 1998) and the duration of extensional magmatism between *ca.* 40 Ma and 30 Ma (e.g., Zhang and Schiirer, 1999; Chen et al., 2019; Pham et al., 2020) are likely to support the short-lived granulite-facies metamorphism. The preservation of prograde zoning in a garnet porphyroblast of granulite-facies pelitic gneiss (Figs. 6a-b) in this study is probably consistent with the hypothesis. As suggested by Dinh et al. (2023), the continued crustal thinning linked with the seafloor spreading of the East Sea might have caused the D_2 event at *ca.* 31–29 Ma (Table 3). Eventually, the strike-slip shearing of the RRSZ synchronous with a D_3 doming event probably happened at *ca.* 27–25 Ma under a geothermal gradient of *ca.* 60°C/km (Table 3).

Table 3. Schema of metamorphic-deformation stages in the Day Nui Con Voi metamorphic complex

Metamorphic stage	Metamorphic condition	Deformation event		Tectonics	East Sea	Period
Prograde	kyanite-grade amphibolite-facies 20–25 °C/km	D0	?	India–Asia collision		> 40 Ma
	sillimanite-grade upper amphibolite- to granulite-facies	D1	upright folding			
Peak	suprasolidus sillimanite-grade granulite-facies *ca.* 30 °C/km			extensional magmatism	initila back-arc magmatism	*ca.* 40–30 Ma
Retrograde	suprasolidus sillimanite-grade upper amphibolite- to granulite-facies?	D2	subhorizontal folding	crustal thinning	opening	*ca.* 31–29 Ma
	sillimanite-andalusite transition lower amphibolite- to upper greenschist-facies *ca.* 60 °C/km	D3	doming	strike-slip shearing		*ca.* 27–25 Ma
	andalusite-grade? greenschist-facies?			further uplifting	ridge jump	~20 Ma

Data source: Nam et al. (1998), Wang et al. (1998, 2000), Leloup et al. (2001), Garnier et al. (2002), Gilley et al. (2003), Yeh et al. (2008), Palins et al. (2013), Mai et al. (2018), Chen et al. (2019), Dinh et al. (2023)

Before the RRSZ shearing activity, extensive leucogranite was produced by partial melting and crustal thinning during granulite-facies metamorphism and may have contributed to crustal weakening both thermally and rheologically, as suggested by previous studies (e.g., Chen et al., 2023; Dinh et al., 2023, and references therein). The Late Eocene extensional magmatism which led the granulite-facies metamorphism and extensive partial melting is likely to have happened almost parallel to the Neotethys subduction trench due to inducing by the back-arc extension setting. Thus, the continental and oceanic crusts were regionally weakened along the hot zone formed by Late Eocene extensional magmatism. This might have become a pathway for the later strike-slip shearing of the RRSZ in the continental crust and for the initial ridge development of the East Sea in the oceanic crust. The shearing maybe further affected the uplift of the DNCV and the southward ridge jump in the East Sea (Table 3). However, the speculative tectonic

evolution of the DNCV requires demonstration through precise and comprehensive geochronological work. In this study, ubiquitous tourmaline crystals were identified in pelitic schists and gneisses, as well as in associated leucogranites. (Figs. 4b-d), which are rarely reported from the DNCV. Furthermore, the first discovery of an aluminous borosilicate mineral, dumortierite, from the granite in Nam Dinh (Figs. 4g-h) may reflect a unique boron-enriched environment for its formation through fluid (+ melt)–rock interaction. Further petrological investigation, focusing on these borosilicate minerals as fluid recorders, will also provide valuable insights into fluid activities and their implications for the tectonic evolution of the DNCV.

7. Conclusions

This study conducted a field survey of small outcrops around Nam Dinh, northern Vietnam, which corresponds to the southeasternmost part of the Day Nui Con Voi metamorphic complex. Apart from a minor occurrence of sandstone, possibly representing part of the Triassic sedimentary formation, the petrographical features of the dominant pelitic schists/gneisses reveal a metamorphic zonation from the chlorite zone through the biotite–muscovite zone to the sillimanite zone, reflecting an increase in metamorphic grade toward the east. The clockwise *P–T* trajectory, characterized by peak granulite-facies anatexis and structural features such as dominant subhorizontal foliation and mylonitization, is consistent with those of the Day Nui Con Voi metamorphic complex. Integrating the thermal histories of not only the metamorphic complex but also the Bu Khang Dome and the Phan Si Pan zone, adjacent to the study area, and the East Sea, provided insight into the regional tectonothermal evolution during the Eocene–Oligocene. The India-Asia collision in Eocene led to prograde metamorphism with a 20–25°C/km geotherm, followed by crustal thinning and extensional magmatism before the initial opening of the East Sea. This extension triggered the peak granulite-facies metamorphism and extensive crustal anatexis, accompanied by a geotherm of approximately 30°C/km. Further thinning of the melted crust by the opening of the East Sea promoted the uplift and weakening of the lower crust. Eventually, the strike-slip shearing along the weakening crust in the Red River Shear Zone likely occurred, resulting in the doming and subsequent uplift of the Day Nui Con Voi metamorphic complex and the southern ridge jump of the East Sea.

Acknowledgements

We thank two anonymous reviewers for constructive reviews, which significantly improved the manuscript, and T.T. Phan for the editorial handling. We also acknowledge H.L. Vu for his kind support during the fieldwork, T. Otake and R. Kikuchi for making the scanning electron microscope and Raman spectroscopy available for our use, and A. Matsumoto for supporting the electron microprobe analysis. This study was partly supported by the Vietnam National Foundation for Science and Technology Development (NAFOSTED) under grant number 105.99-2023.10.

References

Anczkiewicz R., Viola G., Müntener O., Thirlwall M.F., Villa I.M., Quong N.Q., 2007. Structure and shearing conditions in the Day Nui Con Voi massif: Implications for the evolution of the Red River shear zone in northern Vietnam. Tectonics, 26, TC2002.

Aoya M., Kouketsu Y., Endo S., Shimizu H., Mizukami T., Nakamura D., Wallis S., 2010. Extending the applicability of the Raman carbonaceous material geothermometer using data from contact metamorphic rocks. Journal of Metamorphic Geology, 28, 895–914.

Bui T.S.V., Osanai Y., Lenz C., Nakano N., Adachi T., Belousova E., Kitano I., 2019. Gem-Quality Zircon

Megacrysts from Placer Deposits in the Central Highlands, Vietnam Potential Source and Links to Cenozoic Alkali Basalts. Minerals, 9, 89.

Chen X., Burg J.-P., Liu J., Qi Y., Fan W., Wang K., 2019. Multistage Remobilization of the Southwestern Margin of the South China Plate: Insights From Zircon U-Pb Geochronology and Hf Isotope of Granitic Rocks From the Yao Shan Complex, Southeastern Tibet Plateau. Tectonics, 38, 621–640.

Chen X., Liu J., Burg J.-P., Yan J., Zhou B., Shan H., Bao X., Fan W., Zhang J., Hou C., 2023. Lateral middle-lower crustal flow in response to continental collision: New insights from the metamorphic complexes in the southeastern Tibetan Plateau. Earth-Science Reviews, 247, 104604.

Chung S.-L., Lee T.-Y., Lo C.-H., Wang P.-L., Chen C. -Y., Yem N.T., Hoa T.T., Genyao W., 1997. Intraplate extension prior to continental extrusion along the Ailao Shan-Red River shear zone. Geology, 25(4), 311–314.

Dinh M.M., 2004. Ninh Binh. Geological and Mineral Resources map of Viet Nam 1:200,000. Department of Geology and Minerals of Viet Nam, Ha Noi.

Dinh T.H., Yeh M.W., Lee T.Y., Kunk M.J., Wintsch R.P., McAleer R., 2023. Extrusion tectonism of Indochina reassessed: constraints from $^{40}Ar/^{39}Ar$ geochronology from the Day Nui Con Voi metamorphic massif, Vietnam. Frontiers in Earth Science, 11, 1125279.

Duong V.-H., Trinh P.T., Nguyen T.-D., Piestrzyski A., Nguyen D.C., Pieczonka J., Ngo X.D., Van P.T., Pham B.T., Nguyen-Van H., Van L.N., Bui D.T., Khac D.V., Bui C.T., 2021. Cu-Au mineralization of the Sin Quyen deposit in north Vietnam A product of Cenozoic left-lateral movement along the Red River shear zone. Ore Geology Reviews, 132, 104065.

Ferry J.M.T., Spear F.S., 1978. Experimental calibration of the partitioning of Fe and Mg between biotite and garnet. Contribution to Minerology and Petrology, 66(2), 113–117.

Garnier V., Giuliani G., Maluski H., Ohnenstetter D., Trong T.P., Quang V.H., Van L.P., Can T.V., Schwarz D., 2002. Ar–Ar ages in phlogopites from marble-hosted ruby deposits in northern Vietnam: evidence for Cenozoic ruby formation. Chemical Geology, 188, 33–49.

Gilley L.D., Harrison T.M., Leloup P.H., Ryerson F.J., Lover O.M., Wang J.H., 2003. Direct dating of left-lateral deformation along the Red River shear zone, China and Vietnam. Journal of Geophysical Research, 108, B2, 2127.

Grambling J.S, 1990. Internally-consistent geothermometry and H_2O barometry in metamorphic rocks The example garnet-chlorite-quartz. Contribution to Minerology and Petrology, 105, 617–628.

Harley S.L., 2016. A matter of time: The importance of the duration of UHT metamorphism. Journal of Mineralogical and Petrological Sciences, 111, 50–72.

Hoang N.K., 1999. Nam Dinh. Geological and Mineral Resources map of Viet Nam 1:200000. Department of Geology and Minerals of Viet Nam, Ha Noi.

Hodges K.V., Crowley P.D., 1985. Error estimation in empirical geothermometry and geobarometry for pelitic systems. American Mineralogist, 70, 702–709.

Hodges K.V., Spear F.S., 1982. Geothermometry, geobarometry and the Al_2SiO_5 triple point at Mt Moosilauke, New Hampshire. American Mineralogist, 67, 1118–1134.

Hoisch T.D., 1990. Empirical calibration of six geobarometers for the mineral assemblage quartz + muscovite + biotite + plagioclase + garnet. Contribution to Minerology and Petrology, 104, 225–234.

Holdaway M.J., 2001. Recalibration of the GASP geobarometer in light of recent garnet and plagioclase activity models and versions of the garnet-biotite geothermometer. American Mineralogist, 86, 1117–1129.

Holdaway M.J., Lee S.M., 1977. Fe-Mg cordierite stability in high-grade pelitic rocks based on experimental, theoretical, and natural observation. Contribution to Minerology and Petrology, 63, 175–198.

Jolivet L., Maluski H., Beyssac O., Goffé B., Lepvrier C., Tri P.T., Vuong N.V., 1999. Oligocene-Miocene Bu Khang extensional gneiss dome in Vietnam: Geodynamic implications. Geology, 27(1), 67–70.

Jolivet L., Beyssac O., Goffé B., Avigad D., Lepvrier C., Maluski H., Thang T.T., 2001. Oligocene-Miocene

midcrustal subhorizontal shear zone in Indochina. Tectonics, 20(1), 46–57.

Kohn M.J., 2014. “Thermoba-Raman-try”: Calibration of spectroscopic barometers and thermometers for mineral inclusions. Earth and Planetary Science Letters, 388, 187–196.

Kouketsu Y., Nishiyama T., Ikeda T., Enami M., 2014. Evaluation of residual pressure in an inclusion–host system using negative frequency shift of quartz Raman spectra. American Mineralogist, 99, 433–442.

Kriegsman L.M., Hensen B.J., 1998. Back reaction between restite and melt: Implications for geothermobarometry and pressure-temperature paths. Geology, 26(12), 1111–1114.

Le Breton N., Thompson A.B., 1988. Fluid-absent (dehydration)melting of biotite in metapelites in the early stages of crustal anatexis. Contributions to Mineralogy and Petrology, 99, 226–237.

Leloup P.H., Lacassin R., Tapponnier P., Schärer U., Zhong D., Liu X., Zhang L., Ji S., Trinh P.T., 1995. The Ailao Shan-Red River shear zone (Yunnan, China), Tertiary transform boundary of Indochina. Tectonophysics, 251, 3–84.

Leloup P.H., Amaud N., Lacassin R., Kienast, J.R., Harrison, T.M., Phan, T.T., Replumaz, A., Tapponnier, P., 2001. New constraints on the structure, thermochronology, and timing of the Ailao Shan-Red River shear zone, SE Asia. Journal of Geophysical Research, 106(B4), 6683–6732.

Mai H.A., Chan Y.L., Yeh M.W., Lee T.Y., 2018. Tectonic implications of Mesozoic magmatism to initiation of Cenozoic basin development within the passive South China Sea (East Sea) margin. International Journal of Earth Sciences, 107, 1153–1174.

Maluski H., Lepvrier C., Jolivet L., Carter A., Roques D., Beyssac O., Tang T.T., Thang N.D., Avigad D., 2001. Ar–Ar and fission-track ages in the Song Chay Massif: Early Triassic and Cenozoic tectonics in northern Vietnam. Journal of Asian Earth Sciences, 19, 233–248.

Nagy E.A., Schärer U., Minh N.T., 2000. Oligo-Miocene granitic magmatism in central Vietnam and implications for continental deformation in Indochina. Terra Nova, 12(2), 67–76.

Nam T.N., Torium M., Itaya T., 1998. *P–T–t* paths and post-metamorphic exhumation of the Day Nui Con Voi shear zone in Vietnam. Tectonophysics, 290, 299–318.

Newton R.C., Haselton H.T., 1981. Thermodynamics of the garnet-plagioclase-Al_2SiO_5-quartz geobarometer. In: Newton, R.C., Navrotsky, A., Wood, B.J. (Eds.), Thermodynamics of Minerals and Melts. Springer-Verlag, New York, 131–147.

Osanai Y., Nakano N., Owada M., Tran N.N., Miyamoto T., Nguyen T.M., Nguyen V.N., Tran V.T., 2008. Collision zone metamorphism in Vietnam and adjacent Southeastern Asia: Proposition for Trans Vietnam Orogenic Belt. Journal of Mineralogical and Petrological Sciences, 103, 226–241.

Palin R.M., Searle M.P., Waters D.J., Parrish R.R., Roberts N.M.W., Horstwood M.S.A., Yeh M.W., Chung S.L., Anh T.T., 2013. A geochronological and petrological study of anatectic paragneiss and associated granite dykes from the Day Nui Con Voi metamorphic core complex, North Vietnam: constraints on the timing of metamorphism within the Red River shear zone. Journal of Metamorphic Geology, 31, 359–387.

Passchier C.W., Trouw R.A.J., 2005. In: Microtectonics. Springer, Berlin, p.366.

Perchuk L.L., 1991. Derivation of a thermodynamically consistent set of geothermometers and geobarometers for metamorphic and magmatic rocks. In: Perchuk, L.L. (Ed.), Progress in Metamorphic and Magmatic Petrology: A Memorial Volume in Honor of D. S. Korzinskiy. Cambridge University Press, London, 93–111.

Pham T.T., Shellnutt J.G., Tran T.-A., Lee H.-Y., 2020. Petrogenesis of Eocene to early Oligocene granitic rocks in Phan Si Pan uplift area, northwestern Vietnam: Geochemical implications for the Cenozoic crustal evolution of the South China Block. Lithos, 372–373, 105640.

Ranaweera L.V., Perera L.R.K., Hiroi Y., 2007. Blue Dumortierite From, Habarana, Sri Lanka: Field Occurrence and Mineral Chemistry. Journal of Geological Society of Sri Lanka, 12, 53–74.

Roger F., Leloup P.H., Jolivet M., Lacassin R., Trinh P.T., Brunel M., Seward D., 2000. Long and complex thermal history of the Song Chay metamorphic dome (Northern Vietnam) by multi-system geochronology. Tactonophysics, 321, 449–466.

Searle M., Cottle J., 2024. Himalayan Leucogranites:

Field Relationships and Tectonics. Elements, 20(6), 373–380.

Spear F.S., Cheney J.T., 1989. A petrogenetic grid for pelitic schists in the system SiO_2-Al_2O_3-FeO-MgO-K_2O-H_2O. Contributions to Mineralogy and Petrology, 101, 149–164.

Spear F.S., Kohn M.J., Cheney J.T., 1999. P–T paths from anatectic pelites. Contributions to Mineralogy and Petrology, 134, 17–32.

Stormer J.C., 1975. Practical two-feldspar geothermometer. American Mineralogist, 60, 667–674.

Stormer J.C., Whitney J.A., 1985. Two feldspar and iron-titanium oxide equilibria in silicic magmas and the depth of origin of large volume ash-flow tuffs. American Mineralogist, 70(1–2), 52–64.

Tapponnier P., Peltzer G., Le Dalin A.Y., Cobbold P., 1982. Propagating extrusion tectonics in Asia: New insights from simple experiments with plasticine. Geology, 10(12), 611–616.

Thompson A.B., 1976. Mineral reactions in pelitic rocks; II, Calculation of some PTX (Fe-Mg) phase relations. American Journal of Science, 276, 425–454.

Travin A., Murzintsev N., Kruk N., 2024. Thermochronology of the Laojunshan-Song Chai Granite Gneiss Massif (North Vietnam, South China). Minerals, 14, 251.

Trinh P.T., Leloup P.H., Robin L., Nicolas A., 1998. Formation of Ruby in the Red River metamorphic zone. Proceedings of the NCST of Vietnam, 10(1), 143–148.

Wang P.-L., Lo C.-H., Lee T.-Y., Chung S.-L., Lan C.-Y., Yem N.T., 1998. Thermochronological evidence for the movement of the Ailao Shan-Red River shear zone: A perspective from Vietnam. Geology, 26(10), 887–890.

Wang P.-L., Lo C.-H., Chung S.-L., Lee T.-Y., Lan C.-Y., Thang T.V., 2000. Onset timing of left-lateral movement along the Ailao Shan-Red River Shear Zone: $^{40}Ar/^{39}Ar$ dating constraint from the Nam Dinh Area, northeastern Vietnam. Journal of Asian Earth Sciences, 18, 281–292.

Warr L.N., 2021. IMA-CNMNC approved mineral symbols. Mineralogical Magazine, 85, 291–320.

Wu C.M., 2017. Calibration of the garnet-biotite-Al_2SiO_5-quartz geobarometer for metapelites. Journal of Metamorphic Geology, 35(9), 983–998.

Yeh M.W., Lee T.Y., Lo C.H., Chung S.L., Lan C.Y., Anh T.T., 2008. Structural evolution of the Day Nui Con Voi metamorphic complex: Implications on the development of the Red River Shear Zone, Northern Vietnam. Journal of Structural Geology, 30, 1540–1553.

Zhang L.S., Schärer U., 1999. Age and origin of magmatism along the Cenozoic Red River shear belt, China. Contributions to Mineralogy and Petrology, 134, 67–85.

Zhong W., Andersen N.H., Dabrowski M., Jamtveit B., 2019. Zircon and quartz inclusions in garnet used for complementary Ramanthermobarometry: application to the Holsnøy eclogite, Bergen Arcs,Western Norway. Contributions to Mineralogy and Petrology, 174, 50.